

INTERNAL KINEMATICS OF THE FORNAX DWARF SPHEROIDAL GALAXY

MATTHEW G. WALKER AND MARIO MATEO

Department of Astronomy, University of Michigan, 830 Dennison Building, Ann Arbor, MI 48109-1042;
mgwalker@umich.edu, mmateo@umich.edu

EDWARD W. OLSZEWSKI

Steward Observatory, University of Arizona, 933 North Cherry Avenue, Tucson, AZ 85721; eolszewski@as.arizona.edu

REBECCA BERNSTEIN

Department of Astronomy, University of Michigan, 830 Dennison Building, Ann Arbor, MI 48109-1042; rabernst@umich.edu

AND

XIAO WANG AND MICHAEL WOODROOFE

Department of Statistics, University of Michigan, 1085 South University, Ann Arbor, MI 48109;
wangxiao@umich.edu, michaelw@umich.edu

Received 2005 June 10; accepted 2005 November 15

ABSTRACT

We present new radial velocity results for 176 stars in the Fornax dwarf spheroidal galaxy, of which at least 156 are probable Fornax members. We combine with previously published data to obtain a radial velocity sample with 206 stars, of which at least 176 are probable Fornax members. We detect the hint of rotation about an axis near Fornax’s morphological minor axis, although the significance of the rotation signal in the galactic rest frame is sensitive to the adopted value of Fornax’s proper motion. Regardless, the observed stellar kinematics is dominated by random motions, and we do not find kinematic evidence of tidal disruption. The projected velocity dispersion profile of the binned data set remains flat over the sampled region, which reaches a maximum angular radius of $65'$. Single-component King models in which mass follows light fail to reproduce the observed flatness of the velocity dispersion profile. Two-component (luminous plus dark matter) models can reproduce the data, provided that the dark component extends sufficiently beyond the luminous component and the central dark matter density is of the same order as the central luminous density. These requirements suggest a more massive, darker Fornax than standard core-fitting analyses have previously concluded, with M/L_V over the sampled region reaching 10–40 times the M/L_V of the luminous component. We also apply a nonparametric mass estimation technique, introduced in a companion paper. Although it is designed to operate on data sets containing velocities for >1000 stars, the estimation yields preliminary results suggesting $M/L_V \sim 15$ inside $r < 1.5$ kpc.

Key words: galaxies: dwarf — galaxies: individual (Fornax) — galaxies: kinematics and dynamics — Local Group — methods: statistical — techniques: radial velocities

Online material: machine-readable tables

1. INTRODUCTION

The Milky Way’s dwarf spheroidal (dSph) satellite galaxies have stellar masses similar to those of globular clusters ($M_{\text{luminous}} \sim 10^6 - 10^7 M_{\odot}$), yet they are much more spatially extended ($R \sim 0.5 - 3$ kpc for dSphs; $R \sim 0.01 - 0.05$ kpc for globular clusters). These characteristics give dSphs the lowest luminosity densities of any known galaxies. The discovery that their internal velocity dispersions all exceed 7 km s^{-1} (Aaronson 1983; Mateo 1998 and references therein) has given rise to competing interpretations and speculations concerning their origin and cosmological significance.

If dSphs are assumed to be approximately virialized systems, their large velocity dispersions indicate the presence of copious amounts of dark matter. Estimates of mass-to-light ratios (M/L) based on the equilibrium assumption have yielded $M/L \sim 5 - 500$ in solar units for various Milky Way dSphs (Mateo 1998 and references therein; Kleyna et al. 2001, 2005; Odenkirchen et al. 2001). The dSphs are then the smallest, nearest systems believed to reside within dark matter halos and so provide a convenient and fundamental testing ground for cold dark matter models of structure formation.

Alternatively, large measured velocity dispersions have been cited as possible evidence that the dSphs are currently undergoing tidal disruption as they orbit within the Milky Way potential (Kuhn 1993; Kroupa 1997; Klessen & Kroupa 1998; Klessen & Zhao 2002; Fleck & Kuhn 2003). According to this interpretation, dSphs may be in a state far from dynamical equilibrium, and masses derived under that assumption may be inflated. If the observed stellar velocity dispersions can be attributed to streaming tidal debris projected along the line of sight, the need to invoke dark matter for explaining dSph kinematics subsides, perhaps entirely (Fleck & Kuhn 2003; Kroupa 1997).

Large samples of radial velocities measured for dSph stars may be capable of distinguishing between various equilibrium and tidal models by examining the velocity trends across the face of the system. If a dSph is close to dynamical equilibrium, its stellar motions provide an estimate of the underlying mass distribution. Tidal disruption is expected to be accompanied by a radial velocity gradient, giving rise to apparent rotation with a characteristic orientation. We present in this paper new radial velocity results for 176 stars along the line of sight to Fornax. After combining with previously published results, we test for rotation and then measure the radial velocity dispersion profile

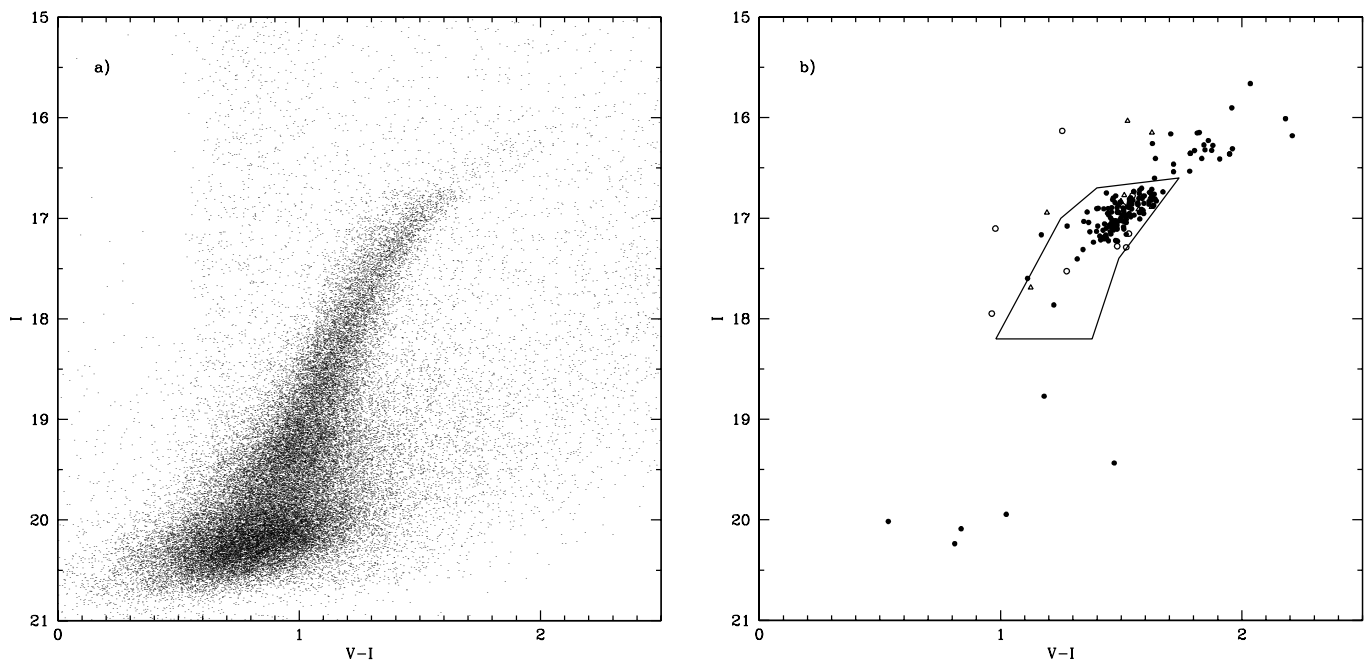


FIG. 1.—Fornax RGB. (a) Plot including all stars measured photometrically in a $130' \times 110'$ region of sky centered on the Fornax dSph. (b) Plot showing only those stars observed spectroscopically and illustrating the boundaries of our color-magnitude target selection region. Filled circles are probable Fornax members, based on velocity criteria described in § 3.2. Open circles are probable foreground contaminants. Open triangles represent stars with marginal membership status. Points located outside the CMD selection region represent stars observed for this study before the photometry making up this CMD was available, and so they were chosen based on the photometry described in M91.

extending from the Fornax center to the edge of the luminous component. We consider the results in the contexts of equilibrium and tidal disruption models. We also estimate the Fornax mass nonparametrically, applying a technique formally introduced in a companion paper by Wang et al. (2005, hereafter Paper I).

2. OBSERVATIONS AND DATA REDUCTION

2.1. Photometry, Astrometry, and Target Identification

In order to identify spectroscopic target stars, we first obtained photometric data from 31 fields covering a $130' \times 110'$ region of sky centered on the Fornax dSph ($\alpha_{J2000.0} = 02^{\text{h}}39^{\text{m}}52^{\text{s}}$, $\delta_{J2000.0} = -34^{\circ}28'09''$). These observations took place the nights of 1993 November 30, December 1, and December 10, during photometric conditions. The data consist of 600–700 s exposures in both V and I filters using the 2048×2048 TEK 3 CCD detector at the Las Campanas Observatory 40 inch (1.02 m) telescope (field size = $24' \times 24'$, scale = $0''.7$ pixel $^{-1}$). The images were processed using twilight flat-field exposures and multiple bias frames. We used the two-dimensional stellar photometry program DoPHOT (Schechter et al. 1993) for the reductions and placed the resulting instrumental magnitudes on the Kron-Cousins scale (Bessell 1976) using 56 Landolt photometric standard stars observed during the same nights. From the formal error values returned by DoPHOT and multiple measurements of stars in overlapping field regions, we estimate our photometric accuracy to be $\pm 3\%$.

The resulting color-magnitude diagram (CMD) is shown in Figure 1, which also shows the region in the CMD from which we selected stars for spectroscopic observation. The boundaries of this region were chosen to enclose points representing likely Fornax members, as well as those stars bright enough to maintain reasonable integration times during spectroscopy. The chosen region roughly extends along the brightest ~ 1.5 I -band magnitudes of the Fornax red giant branch (RGB) and includes more than

4000 Fornax candidate members. We conservatively chose from among the brighter targets in this selection region for spectroscopic follow-up. Based on our spectroscopy results, it is feasible to derive accurate radial velocities for stars at even the faint edge of this selection region.

Since one of our spectroscopic observing runs took place prior to 1993, some targets were selected without the benefit of this photometry. For target identification leading up to the 1992 November–December spectroscopy run, we relied on photometry obtained in 1990 November over a smaller region of sky. Reduction of these photometric data is described in Mateo et al. (1991, hereafter M91). Many of these targets fall outside the selection region shown in Figure 1b. This earlier effort was devoted to observing primarily the brightest candidate members, although several faint RGB stars were selected in order to probe the limits of the instrumentation.

An additional factor entering our target selection was a star's sky position relative to the center of Fornax. To aid this selection, we converted the (x, y) CCD position returned by the DoPHOT centroid algorithm into equatorial coordinates using the IRAF routines TFINDER and CCTRANS and tied our astrometry to the USNO-1B system using up to several hundred USNO stars per CCD frame. From measurements of stars in overlapping fields, we estimate the 2σ astrometric accuracy to be better than $0''.2$. In deciding on eventual spectroscopic targets, a selection routine closely following the stellar density distribution is inadequate. The outer, sparsely populated regions are of disproportionately high kinematic interest. Nevertheless, we wished to obtain a large sample with a high fraction of Fornax members. In the end we chose at least two to three candidate members in all of the outer Fornax CCD fields and limited our selection in the inner fields to approximately five to eight stars per field. Figure 2 maps the locations of the stars falling within our CMD selection region and identifies which of those stars we ultimately observed spectroscopically.

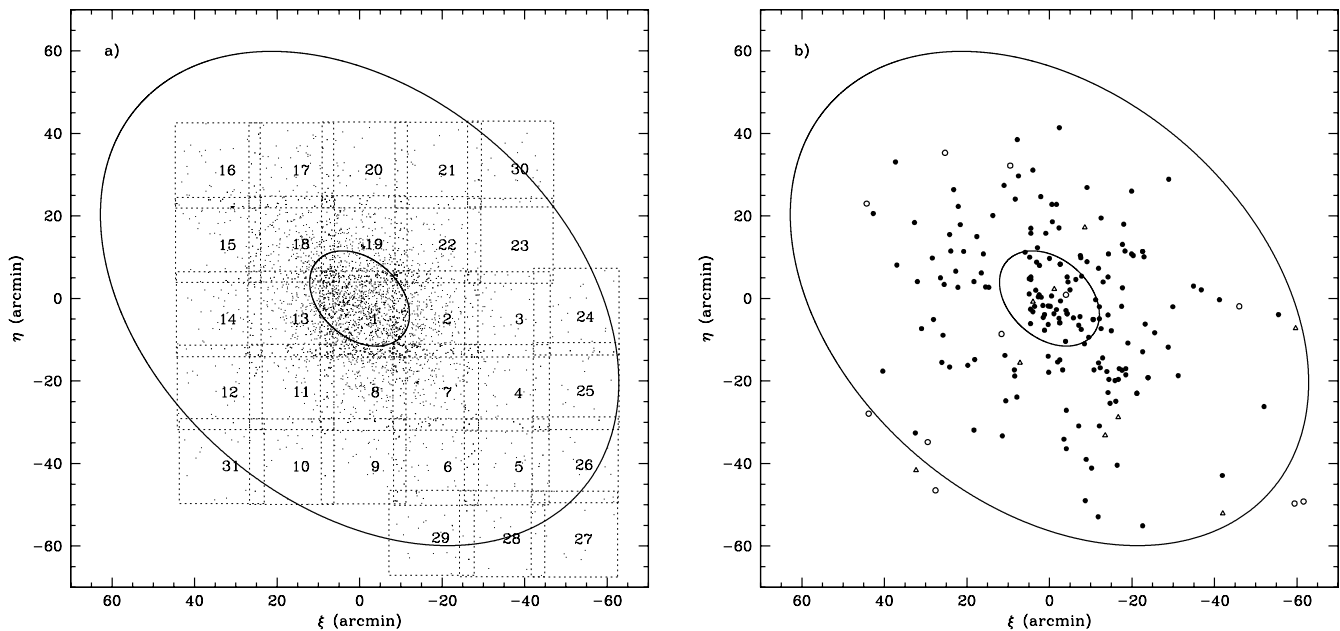


FIG. 2.— (a) Maps of all stars meeting the selection criteria discussed in § 3.2; overplotted are the boundaries of the 31 photometric fields observed. (b) Maps of stars for which we measured radial velocities. Filled circles represent stars later determined to be probable Fornax members. Open circles represent stars rejected as probable foreground contaminants on the basis of their radial velocities. Open triangles represent stars having velocities marginally consistent with Fornax membership (see § 3.2). The inner and outer ellipses are the King core and tidal radii, respectively, which have published semimajor axis values $r_{\text{core}} = 13.7 \pm 1.2$ and $r_{\text{tide}} = 71.1 \pm 4.0$, with ellipticity $e = 0.30 \pm 0.01$ (IH95). The standard coordinate system is centered on the Fornax dSph such that $(\xi, \eta) = (0, 0)$ corresponds to $\alpha_{J2000.0} = 02^{\text{h}}39^{\text{m}}52^{\text{s}}$, $\delta_{J2000.0} = -34^{\circ}28'09''$. North is toward the top of the figure, east is to the left.

2.2. Spectroscopy

We obtained spectra of the selected red giants over four observing runs occurring 1992 November 28–December 7, 1993 December 12–20, 1994 October 22–28, and 2002 December 12–15. The 1992–1994 spectra were taken at the Las Campanas Observatory 2.5 m du Pont Telescope equipped with an echelle spectrograph and 2D-Fruitti photon counting detector (Shectman 1984). The 2002 spectra were acquired at the Magellan 6.5 m Clay Telescope with the Magellan Inamori Kyocera Echelle (MIKE) spectrograph (Bernstein et al. 2003) using a $1'' \times 5''$ slit and MIKE’s red-side CCD detector set to obtain spectra between 4400 and 8000 Å. As they came from different telescopes/instruments, the 1992–1994 spectra and 2002 spectra were reduced independently. We followed the same general procedure in both cases. In what follows, we describe the observation and reduction procedure specific to the 2002 spectra. Where details differ regarding the 1992–1994 spectra, we comment parenthetically.

Object exposure times were in the range 360–720 s (900–2400 s for the 1992–1994 runs), with most at 600 s (1800 s). In addition, we took 1 s (360 s) exposures of a Th-Ar comparison arc lamp before and after object exposures. Other exposures included quartz-illuminated dome flats and spectra of bright radial velocity standard stars used for aperture identification and velocity calibration. We used the IRAF data reduction software package to reduce the raw spectra to heliocentric radial velocities. After overscan and bias subtraction, we produced a master flat-field frame for each night by averaging quartz-illuminated dome exposures. Flat-field frames were then normalized using the IRAF task APFLATTEN, which models and removes both the spatial profile and spectral shape of the illumination pattern, leaving only the sensitivity variations. We corrected our object spectra for these sensitivity variations by dividing each by the appropriate normalized flat-field frame. We then ran the IRAF task APALL (with FORMAT keyword set to “strip”) on the

spectra of the bright standard stars to obtain two-dimensional traces of the echelle orders on the detector and rectify the spectra. We found the order location on the detector to remain quite stable over the course of the run (MIKE is fixed with respect to gravity). We then ran APALL on all the target object spectra to obtain a rectified spectrum from each order, referencing the trace pattern identified for the most recently observed bright star. Thorium-argon comparison spectra were rectified in exactly the same manner as the individual stellar spectra they would eventually correct and calibrate.

For the 2002 data we had also to remove cosmic rays (the 1992–1994 data obtained via the photon-counting device did not suffer from cosmic rays). As a first pass, we ran the IRAF task COSMICRAYS, specifying conservative thresholds so as to remove only the most conspicuous events. The majority of cosmic rays were then removed by the task CONTINUUM, using a 10th-order cubic spline to replace any pixel value above an upper sigma threshold determined by eye to optimize accurate cosmic-ray identification.

We then employed the tasks IDENTIFY and REIDENTIFY to convert the Th-Ar spectra from pixels to wavelength space. A typical arc lamp spectrum would have, for the 10 orders (4 orders) we eventually used for velocity measurement, 140 lines (320 lines) reidentified with an rms scatter of 0.09 Å (0.03 Å) for a fourth-order polynomial fit to the wavelength solution. These wavelength calibrations were then applied to the object spectra using the DISPCOR task, which converts units in the dispersion direction from pixels to angstroms using the weighted solutions to the two nearest comparison arc spectra as references.

Up to this point, the spectra remained two-dimensional, and we had treated each row in the spatial direction separately. This is necessary because the spatial and spectral axes are not orthogonal within each order (i.e., the spectral lines are tilted by $\sim 20^\circ$ with respect to the spatial direction on the detector). By wavelength calibrating each row in the spatial direction explicitly, we

eliminate this problem and retain the full spectral resolution of the instrument.

We then converted the wavelength-calibrated two-dimensional spectra to one-dimensional spectra (for the 1992–1994 spectra, this was accomplished by the ECDISPCOR subroutine). For the 2002 spectra, first we used SCOMBINE to sum the five spatial rows at the center of each spectral order, which we had determined to carry the stellar signal. Separately, we averaged two rows located sufficiently far from that aperture center so as to identify primarily the sky spectrum. Finally, we used SCOMBINE to subtract the normalized sky spectrum from the summed stellar spectrum of the same aperture. A second pass with CONTINUUM then fitted and subtracted the continuum signal, and IMREPLACE then replaced with zero any pixel with absolute value greater than 50. Our velocity measurements are limited to the wavelength range $\sim 4900\text{--}5600\text{ \AA}$ ($\sim 5120\text{--}5460\text{ \AA}$), to improve precision of the results. The wavelength range chosen for the 1992–1994 data corresponds to the four echelle orders determined to yield the most precise velocity measurements from these spectra. At wavelengths redder than this range, the metal-poor spectra provide few absorption lines, while at wavelengths blueward of 4900 \AA , there is little continuum flux from the red giant targets. The strongest absorption lines within the selected region belong to the magnesium *b*-line triplet having a rest wavelength near 5170 \AA , while the many weaker absorption lines contribute usefully in aggregate to the cross-correlation function.

We calculated heliocentric radial velocities using the cross-correlation package FXCOR. We cross-correlated the extracted spectrum of each target star against a high signal-to-noise ratio template consisting of the sum of 27 (75) spectra of bright radial velocity standard stars. The spectrum for each standard had first been shifted to a common heliocentric redshift equal to that of the star HD 6655 ($v_{\text{helio}} = 19.5 \pm 0.3\text{ km s}^{-1}$; Udry et al. 1999). Prior to cross-correlation, we filtered the 10,970 (8192) pixel spectra with a ramp function, cutting on at 175 (100) wavenumbers, increasing linearly to full value at 200 (170), and then decreasing linearly from 2200 (700) to a cutoff at 2500 (1000). A Gaussian fit then located the center of the cross-correlation peak, thereby specifying the radial velocity difference between the object and template.

2.3. Measurement Uncertainties

As a check on the reliability of the extractions and cross-correlations, we compare independent velocity results obtained for the bright standard stars observed multiple times. Let N_{bright} be the number of standard stars observed, and let N_b be the number of independent observations of standard star *b*. Letting N_B be the total number of individual measurements accumulated for standard stars ($N_B = \sum_{b=1}^{N_{\text{bright}}} N_b$), we then define the cumulative sample variance over all independent measurements of such stars to be $\sigma_{\text{bright}}^2 = (N_B - N_{\text{bright}})^{-1} \sum_{b=1}^{N_{\text{bright}}} \sum_{j=1}^{N_b} (v_{b,j} - \langle v \rangle_b)^2$. For our sample we find $\sigma_{\text{bright}} = 0.89\text{ km s}^{-1}$ ($\sigma_{\text{bright}} = 0.72\text{ km s}^{-1}$) for $N_B = 24$ ($N_B = 107$). This indicates a satisfactory level of internal consistency for our purposes.

To calculate the internal measurement uncertainty, σ_j , associated with each independent velocity measurement, v_j , we assume that multiple measurements of a given star having true velocity v_{true} follow a Gaussian distribution with mean v_{true} and variance σ_j^2 . Multiple measurements will be distributed as $v_{\text{true}} + \sigma_j \epsilon_j$, where ϵ_j is a random variable fixed by measurement and following a Gaussian probability distribution with mean zero and variance unity (a standard normal distribution). For simplicity we estimate $v_{\text{true},i}$, the true velocity of star *i*, from N_i in-

dependent measurements as¹ $\hat{v}_{\text{true},i} = N_i^{-1} \sum_{j=1}^{N_i} v_{ij}$. We make the further assumption that the difference $\hat{v}_{\text{true},i} - v_{\text{true},i}$ is negligible. This assumption is perhaps naive; however, we find for this data set that a rigorous treatment, properly considering the uncertainty in \hat{v}_{true} , gives nearly identical results. With these assumptions we then express the *j*th velocity measurement of star *i* as

$$v_{ij} = \hat{v}_{\text{true},i} + \sigma_{ij} \epsilon_{ij}. \quad (1)$$

We model the σ_{ij} as a function of the Tonry-Davis *R*-value (Tonry & Davis 1979), which FXCOR calculates as the ratio of the selected cross-correlation peak height to the average height of the nonselected peaks. We express the relationship as

$$\sigma_{ij} = \frac{\alpha}{(1 + R_{ij})^x}. \quad (2)$$

This two-parameter model generalizes the original Tonry-Davis formalism, which assumed $x = 1$. We find that we are better able to reproduce the empirical sample variances obtained from repeat measurements by treating x as a free parameter.

The base-10 logarithm of the squared error in the *i*th measurement is then

$$\log \left[(v_{ij} - \hat{v}_{\text{true},i})^2 \right] = 2 \log \alpha - 2x \log(1 + R_{ij}) + \log(\epsilon_{ij}^2). \quad (3)$$

The term $\log(\epsilon_{ij}^2)$ has mean $\langle \log(\epsilon_{ij}^2) \rangle = -0.55$, from Monte Carlo simulations. If we define $\delta_{ij} \equiv \log(\epsilon_{ij}^2) + 0.55$, equation (3) becomes

$$\log \left[(v_{ij} - \hat{v}_{\text{true},i})^2 \right] = 2 \log \alpha - 2x \log(1 + R_{ij}) + \delta_{ij} - 0.55. \quad (4)$$

We then estimate x and α by linear regression using the (R_{ij}, v_{ij}) data from only those stars with repeat measurements and recognizing that the δ_{ij} have mean value $\langle \delta_{ij} \rangle = 0$. Including bright standard stars, our 2002 data contain 25 (139 for the 1992–1994 data) repeat observations of six (19) different stars. From the 1992–1994 data we obtain the estimates $\hat{\alpha} = 6.0\text{ km s}^{-1}$ and $\hat{x} = 0.50$. Because the 2002 observations contain fewer repeats and no repeat observations of low-*R* target stars, we adopt $x = 0.50$ for the 2002 data and then estimate $\hat{\alpha}$ with a least-squares fit to find $\alpha = 7.6\text{ km s}^{-1}$ for the 2002 results. Using the appropriate values for the parameters α and x , we then calculate the uncertainty in each individual velocity measurement using equation (2).

Within the 1992–1994 data, we were able to check the stability of our velocity zero point both night to night and run to run using individual spectra obtained each night for the bright star CPD –35 919, located just west of the Fornax center. Within a given run, the night-to-night scatter in the measured velocity of CPD –35 919 is nearly identical to its estimated internal errors. Comparing the mean velocity measured for this star in each run, we find no significant run-to-run scatter.

Since the 1992–1994 and 2002 spectra were cross-correlated using different template spectra, we corrected for any systematic zero-point velocity difference between the two independent data sets. To accomplish this, we cross-correlated the target spectra from the 2002 run against the radial velocity template used for

¹ We follow the convention by which the estimation of quantity *q* is denoted \hat{q} .

the 1992–1994 data. We found the resulting measured velocities to differ by less than 0.05 km s^{-1} with respect to their values derived from the 1992–1994 velocity template. Finding an equally small discrepancy when cross-correlating the 1992–1994 target spectra against the 2002 template, we take any zero-point velocity offset between the two data sets to be insignificant. To measure the overall zero-point offset of the entire combined data set, we considered the measured velocities of all bright radial velocity standard stars separately, finding a mean discrepancy of $\langle v_{\text{observed}} - v_{\text{published}} \rangle = 1.25 \text{ km s}^{-1}$, which we take to be our zero-point error. Subtracting this value from all our velocity results, we then measure a mean value of $-0.3 \pm 1.2 \text{ km s}^{-1}$ for eight twilight sky spectra (corrected individually for diurnal and annual motions). Thus, we are confident that we have placed the velocities on a true heliocentric zero point.

3. RESULTS

3.1. Heliocentric Radial Velocities

In Table 1 we present the heliocentric radial velocities and formal uncertainties derived from each individual observation. Entries are sorted by date of first observation, with any repeat measurements of the same star listed directly below. Additional information includes the equatorial coordinates, date and time of observation, and the measured $I, V - I$ photometry for each object. The distance R is the angular distance between the center of Fornax, taken from Irwin & Hatzidimitriou (1995, hereafter IH95) to be $\alpha_{J2000.0} = 02^{\text{h}}39^{\text{m}}52^{\text{s}}.3$, $\delta_{J2000.0} = -34^{\circ}28'09''0$, and the projection of the radial position vector on the plane centered on these coordinates. The position angles are defined to be 0° due north at the tangent point and 90° due east. The final column indicates whether we judge the star to be a probable member (“Y”) or nonmember (“N”) of Fornax, based on photometric and velocity criteria (§ 3.2). Several stars present borderline cases for membership, and we mark their membership status with a question mark. If the membership status is other than “Y,” the superscript indicates whether this is due to the star’s photometry (“p”), velocity (“v”), or both (“v, p”). We include all Fornax targets, as well as the bright star CPD –35 919. Table 2 lists the radial velocity results for the observed standards.

We observed several stars on multiple occasions. In subsequent analyses we take the heliocentric radial velocity of each multiply observed star to be the average of that star’s individual velocity measurements weighted by their respective uncertainties. Table 3 gives the weighted mean velocity, χ^2 value, and the probability, $p(\chi^2)$, for stars having multiple measurements. Several of the Fornax stars in our sample have velocities previously published by M91. Table 4 compares our measurements for these stars with those of M91. For 10 of the 13 stars common to both data sets, we find agreement to within the measurement uncertainties. Of the remaining three, two have velocities reported by M91 differing from our measurements by $\sim 2.5 \sigma$, while the third differs by $\sim 10 \sigma$. See § 5 for a discussion on velocity variability and its effects on our results.

3.2. Fornax Membership

We identify and exclude from our sample those stars that are likely to be foreground contaminants. Having passed positional and photometric criteria, these interlopers are best identified as outliers in the observed velocity distribution. The heliocentric radial velocity of Fornax is $\sim 53 \text{ km s}^{-1}$, so the velocity distribution of its stars overlaps that of foreground stars near $v \sim 0 \text{ km s}^{-1}$. This is apparent in Figure 3a, which depicts the distribution of the radial velocities listed in Table 1. As the derived mass of a pressure-

supported system scales as the square of velocity dispersion, it is imperative that we obtain a sample with minimal contamination from nonmembers. In order to accomplish this objectively, we adopt the robust biweight estimator (Beers et al. 1990), which determines a characteristic distribution width, σ_{bw} , equal to the standard deviation in the special case of a normal distribution. Since 99% of the members in a normally distributed sample are located within 2.58σ of the mean, we select as a membership criterion $|v_i - \langle v \rangle| < 2.58 \sigma_{\text{bw}}$ and iteratively remove those stars failing to satisfy this condition. This rejection process converges after four iterations, identifying 20 stars as probable foreground. We are left with a sample of 156 new stars we consider to be members of the Fornax dSph. Their radial velocity distribution is shown in Figure 3b.

On examination of Figure 3a, which specifies the iteration that removes each of the rejected stars, one may reasonably wonder whether iterations 4, 3, and possibly 2 of the rejection algorithm remove what are actually Fornax member stars. The eye is tempted to include the three stars with radial velocities in the range $82.5\text{--}92.5 \text{ km s}^{-1}$ in the wing of the distribution centered on Fornax’s systemic velocity. Reinstating these stars as probable Fornax members and then forcing symmetry on the overall Fornax distribution would argue for the additional reinstatement of the rejected stars falling in the $12.5\text{--}22.5 \text{ km s}^{-1}$ range. Where it is practical, we examine the effects on our results of retaining stars rejected in the second, third, and fourth iterations and note that the true membership of Fornax probably includes some, but perhaps not all, of these stars. Pending a larger data set, we leave the membership status of these borderline cases an open question.

Hereafter we combine our new velocity results with the previously published sample of M91. The 44 stellar velocities measured by M91 were drawn from stars belonging to one of two distinct fields: one centered on the Fornax core, another located along the major axis $25'$ southwest of the center. We recalculate weighted mean velocities for any stars measured multiple times and/or in both data sets, using the quoted uncertainties for each observation. In Figure 3c we show the radial velocity distribution of this combined data set, now consisting of velocities for 206 stars. The algorithm described above for membership determination then rejects (again converging after four iterations) 28 stars as probable foreground, including all 20 of the stars that had been rejected before the addition of the M91 data. The eight additional rejected stars come from M91 alone and were rejected in that study as well. Figure 3d shows the velocity distribution of the 176 stars retained as probable Fornax members. Again, we examine the effect of retaining those stars rejected in iterations 3 and 4 (giving a sample with $N = 182$ members), as well as iterations 2, 3, and 4 (giving $N = 186$ members).

3.3. Rotation and the Proper Motion of Fornax

The relative motion between the Sun and Fornax contributes a velocity component, $v_{\text{rel}}(l, b)$, along the line of sight to each Fornax star. A given star’s galactic rest frame (GRF) radial velocity, $v_{r,\text{GRF}}$, is related to its heliocentric rest frame (HRF) velocity,² $v_{r,\text{HRF}}$, by

$$v_{r,\text{GRF}} = v_{r,\text{HRF}} + v_{\text{rel}}(l, b). \quad (5)$$

A gradient in $v_{\text{rel}}(l, b)$ across the face of an object as large in solid angle as Fornax will tend to produce a spurious gradient in

² In either rest frame, a star’s “radial” velocity is the velocity along the line of sight from the Sun to the star. GRF radial velocities are computed for an observer at the Sun’s location, but at rest with respect to Fornax.

TABLE 1
HELIOCENTRIC RADIAL VELOCITY RESULTS FOR FORNAX TARGET STARS

Star	$\alpha_{J2000.0}$	$\delta_{J2000.0}$	HJD (-2,4000,00.0)	UT Date of Observation	R (arcmin)	P.A. (deg)	I	$V - I$	v (km s ⁻¹)	Member
F1-1	02 38 51.5	-34 35 25.5	48955.6	1992 Nov 29	14.5	120.2	16.18	2.21	55.8 ± 2.7	Y
	02 38 51.5	-34 35 25.5	52623.5	2002 Dec 15	14.5	120.2	16.18	2.21	64.5 ± 2.0	Y
F1-2	02 38 52.3	-34 44 55.3	48955.7	1992 Nov 29	20.8	143.7	16.41	1.64	42.9 ± 2.6	Y
	02 38 52.3	-34 44 55.3	48961.6	1992 Dec 05	20.8	143.7	16.41	1.64	45.2 ± 2.2	Y
F1-3	02 38 59.9	-34 45 26.9	48955.7	1992 Nov 29	20.4	148.1	16.54	1.72	49.6 ± 2.3	Y
F1-4	02 39 53.3	-34 46 02.6	48955.8	1992 Nov 29	17.9	180.7	16.41	1.83	44.7 ± 2.6	Y
	02 39 53.3	-34 46 02.6	52621.6	2002 Dec 13	17.9	180.7	16.41	1.83	43.5 ± 1.7	Y
	02 39 53.3	-34 46 02.6	52622.6	2002 Dec 14	17.9	180.7	16.41	1.83	43.5 ± 1.7	Y
F1-5	02 38 03.0	-34 16 39.1	48956.6	1992 Nov 30	25.3	63.1	16.74	1.55	45.5 ± 2.7	Y
F1-6	02 39 14.4	-34 22 42.0	48957.7	1992 Dec 01	9.5	55.2	16.84	1.53	73.9 ± 2.6	Y
F1-7	02 38 23.7	-34 16 38.5	48957.7	1992 Dec 01	21.6	57.9	17.23	1.45	61.3 ± 2.8	Y
F1-8	02 38 26.5	-34 15 01.6	48957.7	1992 Dec 01	22.0	53.6	17.17	1.44	48.5 ± 2.8	Y
F1-9	02 39 28.1	-34 26 02.2	48957.8	1992 Dec 01	5.4	67.1	16.76	1.63	42.7 ± 2.8	Y
F1-10	02 39 52.3	-34 18 25.5	48958.6	1992 Dec 02	9.7	0.0	17.03	1.48	51.3 ± 2.7	Y
F1-11	02 40 07.2	-34 19 18.1	48958.6	1992 Dec 02	9.4	340.8	16.86	1.57	55.1 ± 2.6	Y
F1-12	02 40 15.3	-34 18 09.2	48958.6	1992 Dec 02	11.1	334.6	16.72	1.58	41.5 ± 2.8	Y
F1-13	02 37 55.8	-34 47 16.0	48958.7	1992 Dec 02	30.7	128.7	16.78	1.63	33.5 ± 2.2	Y
F1-14	02 40 14.1	-34 22 57.9	48958.7	1992 Dec 02	6.9	319.1	17.05	1.46	43.7 ± 2.3	Y
F1-15	02 38 09.0	-34 51 07.1	48958.8	1992 Dec 02	31.3	137.4	16.92	1.58	55.0 ± 2.7	Y
F1-16	02 39 11.1	-34 39 09.0	48959.6	1992 Dec 03	13.9	142.4	16.74	1.62	60.6 ± 2.7	Y
F1-17	02 39 36.8	-34 45 29.7	48959.7	1992 Dec 03	17.6	169.6	16.86	1.54	67.7 ± 2.6	Y
F1-18	02 39 40.0	-34 43 00.9	48959.7	1992 Dec 03	15.1	170.4	16.84	1.50	28.5 ± 2.8	Y
F1-19	02 39 42.7	-34 43 33.4	48959.7	1992 Dec 03	15.5	172.7	16.84	1.62	35.5 ± 2.8	Y
F1-20	02 38 43.5	-34 32 05.5	48959.7	1992 Dec 03	14.7	105.6	16.82	1.47	63.0 ± 2.8	Y
F1-21	02 38 57.9	-34 28 26.7	48959.7	1992 Dec 03	11.2	91.6	16.91	1.43	38.6 ± 2.6	Y
F1-22	02 38 53.6	-34 33 04.8	48959.8	1992 Dec 03	13.1	112.3	16.71	1.63	39.8 ± 2.6	Y
F1-23	02 38 53.8	-34 30 06.8	48959.8	1992 Dec 03	12.2	99.3	16.80	1.59	71.1 ± 2.7	Y
F1-24	02 39 00.7	-34 33 17.0	48960.6	1992 Dec 04	11.8	115.9	16.75	1.44	54.9 ± 2.5	Y
F1-25	02 38 49.3	-34 24 05.2	48960.6	1992 Dec 04	13.6	72.7	16.89	1.53	50.5 ± 2.8	Y
F1-26	02 39 08.0	-34 19 11.8	48960.6	1992 Dec 04	12.8	45.6	17.06	1.43	67.5 ± 2.9	Y
F1-27	02 39 15.8	-34 17 43.2	48960.6	1992 Dec 04	12.9	35.9	17.18	1.41	30.0 ± 2.9	Y
F1-28	02 39 06.1	-34 37 29.7	48960.7	1992 Dec 04	13.3	134.5	16.90	1.45	45.2 ± 2.7	Y
F-M18	02 39 31.5	-34 31 50.9	48961.7	1992 Dec 05	5.7	130.8	16.15	1.82	55.0 ± 2.8	Y
F1-30	02 39 30.6	-34 24 07.8	48961.8	1992 Dec 05	6.0	48.1	16.32	1.85	50.2 ± 2.8	Y
F-M26	02 39 40.1	-34 34 02.3	48963.7	1992 Dec 07	6.4	156.9	16.36	1.79	41.2 ± 2.3	Y
F-M15	02 39 54.0	-34 34 24.3	49333.6	1993 Dec 12	6.3	183.1	15.90	1.96	61.7 ± 1.8	Y
F-M4	02 40 01.8	-34 27 48.1	49333.6	1993 Dec 12	2.0	280.1	16.82	1.63	52.3 ± 2.0	Y
	02 40 01.8	-34 27 48.1	49648.6	1994 Oct 22	2.0	280.1	16.82	1.63	53.4 ± 2.6	Y
F18-1	02 41 17.6	-34 13 07.2	49333.6	1993 Dec 12	23.1	310.4	16.98	1.50	50.0 ± 2.0	Y
F15-1	02 42 10.0	-34 18 16.5	49333.7	1993 Dec 12	30.1	289.0	17.09	1.46	59.4 ± 2.3	Y
F15-2	02 42 51.4	-34 19 54.3	49333.7	1993 Dec 12	37.8	282.4	16.78	1.59	60.9 ± 2.3	Y
F18-2	02 41 47.8	-34 16 37.8	49333.7	1993 Dec 12	26.5	295.7	16.86	1.62	56.7 ± 2.3	Y
F18-3	02 41 49.3	-34 12 38.0	49333.7	1993 Dec 12	28.7	302.6	17.07	1.48	66.4 ± 2.6	Y
F-M20	02 40 05.5	-34 27 43.2	49334.6	1993 Dec 13	2.8	278.9	16.01	2.18	63.7 ± 2.3	Y
F-M1	02 39 39.6	-34 19 52.2	49334.6	1993 Dec 13	8.7	17.5	16.36	1.95	56.3 ± 2.3	Y
F19-2	02 39 41.2	-34 11 05.7	49334.6	1993 Dec 13	17.2	7.7	16.87	1.49	56.1 ± 2.2	Y
F19-3	02 39 10.6	-34 10 54.4	49334.6	1993 Dec 13	19.3	26.6	16.77	1.51	20.1 ± 2.3	? ^u
F20-1	02 39 49.5	-34 05 18.6	49334.6	1993 Dec 13	22.8	1.4	16.97	1.52	57.2 ± 2.7	Y
F17-1	02 40 38.3	-33 55 54.8	49334.7	1993 Dec 13	33.6	343.5	16.78	1.55	134.0 ± 2.7	N ^u
F20-2	02 39 08.6	-34 01 14.0	49334.7	1993 Dec 13	28.4	18.6	16.91	1.40	59.6 ± 2.4	Y
F20-3	02 40 11.7	-33 57 01.3	49334.7	1993 Dec 13	31.4	352.6	17.02	1.48	44.2 ± 2.6	Y
F20-4	02 40 28.4	-33 58 27.6	49334.7	1993 Dec 13	30.6	345.9	16.99	1.54	64.6 ± 2.5	Y
F17-2	02 40 45.6	-34 00 42.7	49334.8	1993 Dec 13	29.6	338.1	16.76	1.64	49.5 ± 2.7	Y
F-M2	02 39 43.8	-34 30 53.5	49335.6	1993 Dec 14	3.2	147.6	16.26	1.63	71.8 ± 2.6	Y
F13-1	02 41 20.8	-34 23 59.1	49335.6	1993 Dec 14	18.7	282.7	16.80	1.57	66.2 ± 2.1	Y
F13-2	02 41 39.8	-34 25 26.2	49335.6	1993 Dec 14	22.3	276.9	19.43	1.47	47.2 ± 2.3	Y
F13-3	02 42 00.3	-34 23 04.9	49335.6	1993 Dec 14	26.9	280.7	16.78	1.48	68.2 ± 2.7	Y
F13-4	02 41 56.0	-34 24 40.1	49335.6	1993 Dec 14	25.7	277.6	16.87	1.53	61.7 ± 2.2	Y
F11-1	02 41 28.6	-34 44 19.0	49335.7	1993 Dec 14	25.6	230.7	16.74	1.67	50.4 ± 2.8	Y
F11-2	02 41 20.4	-34 42 53.5	49335.7	1993 Dec 14	23.4	230.8	16.88	1.63	46.0 ± 2.5	Y
F13-5	02 41 57.7	-34 37 01.5	49335.7	1993 Dec 14	27.3	250.9	16.85	1.48	46.3 ± 2.2	Y
F14-1	02 42 22.8	-34 35 24.0	49335.7	1993 Dec 14	31.8	256.7	16.90	1.40	60.7 ± 2.2	Y
F11-3	02 40 44.0	-34 52 55.3	49335.8	1993 Dec 14	27.0	203.1	16.82	1.55	53.9 ± 2.2	Y
F8-1	02 39 32.3	-34 55 16.1	49336.7	1993 Dec 15	27.4	171.4	16.98	1.52	54.2 ± 2.6	Y

TABLE 1— *Continued*

Star	$\alpha_{J2000.0}$	$\delta_{J2000.0}$	HJD (-2,4000,00.0)	UT Date of Observation	R (arcmin)	P.A. (deg)	I	$V-I$	v (km s ⁻¹)	Member
F10-1	02 41 21.4	-35 00 01.8	49337.6	1993 Dec 16	36.8	209.8	16.94	1.58	54.8 ± 2.8	Y
	02 41 21.4	-35 00 01.8	52620.6	2002 Dec 12	36.8	209.8	16.94	1.58	53.0 ± 2.2	Y
F9-2	02 39 35.1	-35 02 17.4	49337.6	1993 Dec 16	34.3	174.1	17.04	1.52	45.2 ± 2.2	Y
F9-3	02 39 32.2	-35 04 35.2	49337.6	1993 Dec 16	36.7	173.6	16.94	1.59	52.1 ± 2.3	Y
F9-4	02 39 17.9	-34 59 05.6	49337.6	1993 Dec 16	31.7	167.2	16.85	1.57	55.2 ± 2.0	Y
F9-5	02 38 57.8	-34 59 58.7	49337.6	1993 Dec 16	33.7	160.7	16.77	0.68	65.3 ± 2.4	N ^p
F6-1	02 38 32.2	-35 08 30.5	49337.7	1993 Dec 16	43.6	157.9	16.92	1.59	32.9 ± 2.1	Y
F6-3	02 38 46.5	-35 01 22.5	49337.7	1993 Dec 16	35.9	157.9	16.83	1.50	86.2 ± 2.8	? ^v
F6-4	02 38 53.2	-34 59 02.9	49337.7	1993 Dec 16	33.2	158.6	17.03	1.49	47.8 ± 2.4	Y
F9-6	02 39 09.8	-35 17 09.9	49337.7	1993 Dec 16	49.8	170.0	17.14	1.37	68.3 ± 2.5	Y
	02 39 09.8	-35 17 09.9	49651.9	1994 Oct 25	49.8	170.0	17.14	1.37	73.0 ± 2.4	Y
F-M17	02 39 46.5	-34 25 52.7	49338.5	1993 Dec 17	2.6	27.8	16.03	1.53	85.1 ± 2.4	? ^v
	02 39 46.5	-34 25 52.7	49651.6	1994 Oct 25	2.6	27.8	16.03	1.53	86.3 ± 2.4	? ^v
	02 39 46.5	-34 25 52.7	49652.5	1994 Oct 26	2.6	27.8	16.03	1.53	85.5 ± 2.5	? ^v
F2-1	02 37 48.4	-34 36 21.9	49338.6	1993 Dec 17	26.8	108.0	16.75	1.58	50.8 ± 2.6	Y
	02 37 48.4	-34 36 21.9	49338.7	1993 Dec 17	26.8	108.0	16.75	1.58	50.1 ± 2.3	Y
F22-1	02 38 03.0	-34 16 39.1	49338.6	1993 Dec 17	25.3	63.1	16.74	1.55	50.5 ± 2.4	Y
F3-1	02 36 32.5	-34 28 13.8	49338.6	1993 Dec 17	41.2	90.3	17.12	1.47	54.5 ± 2.7	Y
F3-2	02 36 53.9	-34 25 52.6	49338.6	1993 Dec 17	36.8	86.7	16.81	1.53	30.5 ± 2.3	Y
F3-3	02 37 27.2	-34 30 03.3	49338.6	1993 Dec 17	30.0	93.8	16.80	1.63	45.4 ± 2.5	Y
F3-5	02 37 32.4	-34 39 53.5	49338.6	1993 Dec 17	31.1	112.4	16.94	1.49	54.8 ± 2.8	Y
	02 37 32.4	-34 39 53.5	49338.6	1993 Dec 17	31.1	112.4	16.94	1.49	55.9 ± 2.5	Y
F2-2	02 37 59.5	-34 34 15.7	49338.7	1993 Dec 17	24.0	104.9	16.91	1.54	67.4 ± 2.6	Y
F2-3	02 38 02.4	-34 41 00.7	49338.7	1993 Dec 17	26.0	119.8	16.86	1.57	50.9 ± 2.3	Y
F2-4	02 38 19.8	-34 38 54.1	49338.7	1993 Dec 17	21.9	119.5	16.90	1.51	47.8 ± 2.7	Y
F22-3	02 38 52.0	-34 08 39.6	49338.7	1993 Dec 17	23.1	32.6	17.03	1.51	53.1 ± 2.2	Y
F7-2	02 38 09.0	-34 51 07.1	49338.8	1993 Dec 17	31.3	137.4	16.92	1.58	51.1 ± 2.8	Y
F7-3	02 38 30.9	-34 56 54.3	49338.8	1993 Dec 17	33.3	149.9	16.91	1.57	21.4 ± 2.8	? ^v
F-M10	02 40 11.7	-34 31 18.8	49339.6	1993 Dec 18	5.1	231.6	17.01	1.58	56.5 ± 2.2	Y
F-M6	02 39 59.5	-34 32 43.3	49339.6	1993 Dec 18	4.8	197.9	16.15	1.82	31.9 ± 2.0	Y
	02 39 59.5	-34 32 43.3	49652.6	1994 Oct 26	4.8	197.9	16.15	1.82	37.7 ± 2.7	Y
F2-5	02 38 26.3	-34 25 33.7	49339.6	1993 Dec 18	17.9	81.8	16.85	1.54	51.5 ± 2.3	Y
F2-6	02 38 39.2	-34 35 54.8	49339.6	1993 Dec 18	16.9	117.4	16.87	1.63	49.0 ± 2.0	Y
F2-7	02 38 27.5	-34 30 00.6	49339.6	1993 Dec 18	17.6	96.2	16.97	1.51	60.5 ± 2.5	Y
F7-4	02 37 55.8	-34 47 16.0	49339.7	1993 Dec 18	30.7	128.7	16.78	1.63	47.4 ± 2.4	Y
F7-5	02 38 54.3	-34 43 45.6	49339.7	1993 Dec 18	19.7	142.7	16.95	1.44	54.5 ± 2.6	Y
F7-6	02 38 49.5	-34 42 29.7	49339.7	1993 Dec 18	19.3	138.0	16.94	1.46	39.2 ± 2.9	Y
F-M8	02 39 53.8	-34 29 56.5	49340.6	1993 Dec 19	1.8	190.0	16.70	1.59	51.4 ± 2.3	Y
	02 39 53.8	-34 29 56.5	49653.6	1994 Oct 27	1.8	190.0	16.70	1.59	57.0 ± 2.7	Y
F11-5	02 40 27.0	-34 43 42.8	49340.6	1993 Dec 19	17.1	204.6	16.95	1.50	20.2 ± 2.3	? ^v
F11-6	02 40 33.6	-34 45 26.3	49340.6	1993 Dec 19	19.3	206.1	17.01	1.52	75.2 ± 2.5	Y
F11-7	02 40 33.4	-34 46 57.4	49340.6	1993 Dec 19	20.6	204.1	16.95	1.59	44.6 ± 2.3	Y
F11-8	02 40 30.6	-34 52 01.3	49340.6	1993 Dec 19	25.1	198.2	17.00	1.50	61.1 ± 2.7	Y
F13-7	02 41 12.3	-34 21 53.2	49340.7	1993 Dec 19	17.6	290.7	17.02	1.46	59.2 ± 2.4	Y
F13-8	02 41 42.5	-34 21 28.5	49340.7	1993 Dec 19	23.7	286.2	16.90	1.46	72.4 ± 2.6	Y
F18-4	02 41 39.1	-34 05 50.4	49340.7	1993 Dec 19	31.4	315.2	16.78	1.60	61.2 ± 2.6	Y
F18-5	02 41 36.9	-34 10 12.4	49340.7	1993 Dec 19	28.1	309.6	16.91	1.51	43.1 ± 2.8	Y
F18-6	02 40 58.4	-34 08 02.4	49340.8	1993 Dec 19	24.3	325.8	16.97	1.55	49.7 ± 2.5	Y
F-M26	02 39 40.1	-34 34 02.3	49341.6	1993 Dec 20	6.4	156.9	16.36	1.79	43.8 ± 2.0	Y
	02 39 40.1	-34 34 02.3	49649.6	1994 Oct 23	6.4	156.9	16.36	1.79	40.3 ± 2.5	Y
F19-4	02 39 49.1	-34 09 34.2	49341.6	1993 Dec 20	18.6	2.0	16.90	1.48	36.8 ± 2.7	Y
F19-5	02 40 14.0	-34 11 07.6	49341.6	1993 Dec 20	17.6	345.2	16.94	1.48	50.8 ± 2.7	Y
	02 40 14.0	-34 11 07.6	49341.6	1993 Dec 20	17.6	345.2	16.94	1.48	42.1 ± 3.0	Y
F19-7	02 40 02.5	-34 03 27.2	49341.6	1993 Dec 20	24.8	355.1	16.94	1.51	54.8 ± 2.3	Y
F13-9	02 41 03.8	-34 25 27.1	49341.7	1993 Dec 20	15.0	280.3	17.08	1.40	63.9 ± 2.3	Y
F19-11	02 39 56.4	-34 12 18.6	49341.7	1993 Dec 20	15.9	356.9	16.97	1.45	73.8 ± 2.8	Y
F19-12	02 40 06.5	-34 15 52.5	49341.7	1993 Dec 20	12.6	346.6	16.85	1.59	75.5 ± 2.7	Y
F19-8	02 40 20.8	-34 16 54.2	49341.7	1993 Dec 20	12.7	332.4	16.80	1.47	79.2 ± 2.3	Y
F19-9	02 40 14.2	-34 12 23.6	49341.7	1993 Dec 20	16.4	344.0	17.00	1.52	50.9 ± 2.5	Y
F13-10	02 41 07.3	-34 25 20.5	49341.8	1993 Dec 20	15.7	280.2	17.07	1.45	65.2 ± 2.6	Y
F10-3	02 40 48.0	-35 01 23.9	49648.6	1994 Oct 22	35.2	198.9	17.20	1.44	57.6 ± 2.5	Y
F11-9	02 40 44.7	-34 41 58.2	49648.7	1994 Oct 22	17.5	217.9	17.03	1.51	58.7 ± 2.5	Y
F12-1	02 41 50.2	-34 44 41.5	49648.7	1994 Oct 22	29.4	235.6	17.20	1.43	68.9 ± 2.2	Y
F12-3	02 43 26.1	-34 55 50.0	49648.7	1994 Oct 22	51.9	237.5	17.15	1.53	0.6 ± 2.2	N ^p
F14-3	02 42 27.3	-34 23 58.9	49648.8	1994 Oct 22	32.2	277.2	17.24	1.38	73.3 ± 2.7	Y

TABLE 1—Continued

Star	$\alpha_{J2000.0}$	$\delta_{J2000.0}$	HJD (−2,4000,00.0)	UT Date of Observation	R (arcmin)	P.A. (deg)	I	$V - I$	v (km s ^{−1})	Member
F15-6	02 43 26.1	−34 04 54.7	49648.8	1994 Oct 22	49.9	297.5	17.29	1.52	0.2 ± 2.4	N ^v
F16-3	02 41 54.3	−33 52 45.7	49648.9	1994 Oct 22	43.5	324.4	17.20	1.43	−0.9 ± 2.2	N ^v
F17-4	02 40 32.4	−34 04 04.4	49649.6	1994 Oct 23	25.5	341.0	17.23	1.48	45.1 ± 2.5	Y
	02 40 32.4	−34 04 04.4	49652.7	1994 Oct 26	25.5	341.0	17.23	1.48	55.2 ± 2.8	Y
F17-5	02 41 44.4	−34 01 42.4	49649.6	1994 Oct 23	35.2	318.7	20.02	0.54	48.6 ± 2.7	Y
F20-5	02 40 29.9	−33 49 37.2	49649.7	1994 Oct 23	39.3	348.5	17.13	1.40	26.7 ± 2.2	Y
F-M1	02 39 39.6	−34 19 52.2	49649.8	1994 Oct 23	8.7	17.5	16.36	1.95	51.8 ± 2.8	Y
F20-6	02 39 44.2	−34 05 20.0	49649.8	1994 Oct 23	22.9	4.2	17.07	1.48	28.2 ± 2.2	Y
F20-7	02 39 40.6	−33 46 44.0	49649.8	1994 Oct 23	41.5	3.4	17.10	1.44	47.6 ± 2.5	Y
F-M3	02 39 39.4	−34 28 46.7	49650.5	1994 Oct 24	2.7	103.4	15.66	2.04	57.8 ± 1.8	Y
F-M7	02 39 58.2	−34 32 05.3	49650.6	1994 Oct 24	4.1	197.2	16.89	1.53	41.5 ± 3.0	Y
F21-2	02 37 33.1	−33 59 13.0	49650.6	1994 Oct 24	40.8	45.0	17.16	1.52	50.8 ± 2.1	Y
F22-5	02 38 43.0	−34 17 19.4	49650.7	1994 Oct 24	17.9	53.0	17.12	1.42	58.0 ± 2.2	Y
F22-6	02 38 25.4	−34 10 07.8	49650.7	1994 Oct 24	25.4	45.0	17.10	1.48	66.1 ± 2.6	Y
F22-7	02 38 15.9	−34 17 18.5	49650.8	1994 Oct 24	22.6	61.5	17.11	1.51	43.8 ± 2.0	Y
F22-8	02 38 01.2	−34 18 01.4	49650.8	1994 Oct 24	25.1	66.3	17.14	1.46	68.9 ± 2.6	Y
F23-2	02 37 22.7	−34 21 31.3	49650.8	1994 Oct 24	31.6	78.1	18.42	−0.94	48.7 ± 2.2	N ^p
F3-10	02 37 03.2	−34 25 02.5	49650.9	1994 Oct 24	35.0	85.1	17.09	1.47	71.1 ± 2.8	Y
F-M13	02 40 11.8	−34 28 54.3	49651.5	1994 Oct 25	4.1	259.4	16.15	1.63	89.2 ± 2.3	? ^v
F4-3	02 37 20.2	−34 46 45.9	49651.6	1994 Oct 25	36.4	120.9	17.11	1.48	58.9 ± 2.7	Y
F15-4	02 42 30.2	−34 09 36.2	49652.6	1994 Oct 26	37.5	299.4	17.20	1.42	56.2 ± 2.5	Y
	02 42 30.2	−34 09 36.2	52623.6	2002 Dec 15	37.5	299.4	17.20	1.42	54.2 ± 1.7	Y
F22-4	02 38 54.7	−34 20 50.6	49652.7	1994 Oct 26	13.9	58.5	16.94	1.58	45.5 ± 2.6	Y
F18-11	02 41 09.6	−34 17 21.5	49652.8	1994 Oct 26	19.3	304.0	17.17	1.44	31.7 ± 2.6	Y
F18-9	02 41 32.9	−34 16 44.5	49652.8	1994 Oct 26	23.7	298.7	17.16	1.46	61.0 ± 2.9	Y
F13-13	02 40 48.8	−34 36 43.1	49652.9	1994 Oct 26	14.5	233.6	16.88	1.51	1.9 ± 2.7	N ^v
F24-1	02 35 23.1	−34 31 43.5	49653.6	1994 Oct 27	55.6	94.0	16.83	1.65	61.2 ± 2.3	Y
F24-2	02 35 02.3	−34 34 59.1	49653.6	1994 Oct 27	60.1	96.9	16.89	1.63	15.1 ± 2.5	? ^v
	02 35 02.3	−34 34 59.1	52620.6	2002 Dec 12	60.1	96.9	16.89	1.63	20.7 ± 2.6	? ^v
F26-2	02 36 27.2	−35 10 53.0	49653.7	1994 Oct 27	60.0	135.7	17.00	1.46	58.0 ± 2.6	Y
F27-2	02 35 01.1	−35 17 29.5	49653.7	1994 Oct 27	77.5	129.9	17.10	0.98	4.4 ± 2.9	N ^v
F29-1	02 38 01.6	−35 23 10.4	49653.7	1994 Oct 27	59.5	157.7	16.95	1.53	48.4 ± 2.8	Y
F31-1	02 42 16.3	−35 02 48.7	49653.8	1994 Oct 27	45.6	220.3	16.81	1.62	9.2 ± 2.6	N ^v
F31-3	02 42 07.3	−35 14 33.1	49653.8	1994 Oct 27	54.0	210.7	17.28	1.48	1.4 ± 2.9	N ^v
	02 42 07.3	−35 14 33.1	49653.8	1994 Oct 27	54.0	210.7	17.28	1.48	7.5 ± 2.5	N ^v
	02 42 07.3	−35 14 33.1	52623.6	2002 Dec 15	54.0	210.7	17.28	1.48	7.5 ± 2.5	N ^v
F2-9	02 39 00.7	−34 33 17.0	49653.9	1994 Oct 27	11.8	115.9	16.81	1.64	39.7 ± 2.9	Y
	02 39 00.7	−34 33 17.0	52623.6	2002 Dec 15	11.8	115.9	16.81	1.64	55.3 ± 1.8	Y
F12-2	02 43 09.0	−34 45 36.3	52620.6	2002 Dec 12	44.1	246.4	17.22	1.48	78.0 ± 2.0	Y
F24-1139	02 36 09.2	−34 29 48.5	52620.6	2002 Dec 12	46.0	92.3	17.53	1.27	113.0 ± 2.4	N ^v
F25-2042	02 35 38.8	−34 54 05.5	52620.6	2002 Dec 12	58.2	116.8	17.60	1.11	28.4 ± 2.6	Y
F26-4616	02 34 50.3	−35 16 57.2	52620.6	2002 Dec 12	78.9	128.6	17.95	0.96	123.7 ± 2.6	N ^v
F29-846	02 38 54.3	−35 21 01.9	52620.6	2002 Dec 12	54.2	167.4	17.86	1.22	49.7 ± 2.6	Y
F1-32	02 39 33.0	−34 27 13.5	52621.6	2002 Dec 13	4.1	76.9	16.13	1.26	4.6 ± 1.9	N ^v
F1-33	02 39 41.2	−34 32 56.4	52621.6	2002 Dec 13	5.3	154.5	18.77	1.18	52.2 ± 2.4	Y
F1-34	02 40 14.7	−34 34 16.1	52621.6	2002 Dec 13	7.7	217.0	20.24	0.81	67.8 ± 2.0	Y
F1-35	02 39 54.0	−34 42 11.0	52621.6	2002 Dec 13	14.0	181.4	16.23	1.86	34.1 ± 1.7	Y
F1-36	02 39 17.6	−34 34 38.4	52621.6	2002 Dec 13	9.6	132.3	16.31	1.96	47.5 ± 2.0	Y
F1-37	02 39 15.3	−34 18 12.8	52621.6	2002 Dec 13	12.5	37.6	16.53	1.78	51.2 ± 3.2	Y
F1-38	02 40 04.1	−34 20 10.8	52621.6	2002 Dec 13	8.3	342.9	16.46	1.72	71.9 ± 1.8	Y
F1-39	02 38 14.1	−34 17 41.2	52621.6	2002 Dec 13	22.8	62.8	16.80	1.54	41.4 ± 1.8	Y
F27-775	02 36 26.6	−35 20 03.5	52621.6	2002 Dec 13	66.9	141.1	17.69	1.12	21.5 ± 3.5	? ^v
F1-40	02 39 58.0	−34 35 48.6	52622.6	2002 Dec 14	7.7	188.6	16.33	1.80	48.3 ± 1.7	Y
F1-41	02 39 33.3	−34 38 30.2	52622.6	2002 Dec 14	11.1	159.3	16.41	1.91	49.8 ± 1.5	Y
F1-42	02 39 14.9	−34 35 37.3	52622.6	2002 Dec 14	10.7	134.2	16.27	1.84	38.0 ± 1.9	Y
F1-43	02 39 16.6	−34 32 35.2	52622.6	2002 Dec 14	8.6	121.1	20.09	0.84	59.5 ± 1.8	Y
F1-44	02 38 43.5	−34 22 56.7	52622.6	2002 Dec 14	15.1	69.9	16.94	1.36	81.0 ± 2.9	Y
F1-45	02 39 21.2	−34 23 32.8	52622.6	2002 Dec 14	7.9	54.4	19.94	1.02	65.4 ± 1.8	Y
F1-46	02 39 31.4	−34 22 58.7	52622.6	2002 Dec 14	6.7	39.8	16.28	1.88	56.1 ± 1.5	Y
F1-47	02 39 49.8	−34 27 30.3	52622.6	2002 Dec 14	0.8	39.0	16.33	1.88	48.5 ± 1.7	Y
F1-48	02 40 16.0	−34 23 19.1	52622.6	2002 Dec 14	6.9	314.6	16.60	1.64	55.8 ± 1.7	Y
F14-1805	02 42 08.9	−34 33 07.3	52622.6	2002 Dec 14	28.6	259.8	17.03	1.35	51.5 ± 2.0	Y
F15-2830	02 43 18.8	−34 07 24.0	52622.6	2002 Dec 14	47.4	295.7	17.31	1.34	51.7 ± 2.8	Y
F16-4010	02 42 52.0	−33 54 55.2	52622.6	2002 Dec 14	49.9	311.6	17.08	1.28	55.1 ± 2.4	Y
F1-49	02 39 32.7	−34 31 00.7	52623.6	2002 Dec 15	5.0	125.3	17.23	1.49	60.1 ± 2.0	Y

TABLE 1—*Continued*

Star	$\alpha_{J2000.0}$	$\delta_{J2000.0}$	HJD (−2,4000,00.0)	UT Date of Observation	R (arcmin)	P.A. (deg)	I	$V - I$	v (km s ^{−1})	Member
F1-50.....	02 39 24.4	−34 32 53.1	52623.6	2002 Dec 15	7.5	129.5	16.16	1.71	40.3 ± 1.6	Y
F12-451.....	02 41 59.5	−34 43 34.2	52623.6	2002 Dec 15	30.4	239.3	17.41	1.32	31.0 ± 2.0	Y
F21-3329.....	02 38 16.1	−34 02 05.9	52623.6	2002 Dec 15	32.8	37.5	17.04	1.37	58.2 ± 2.1	Y
F31-1198.....	02 42 30.4	−35 09 37.6	52623.6	2002 Dec 15	52.7	217.8	16.94	1.19	16.8 ± 1.9	? ^v
F31-365.....	02 42 31.0	−35 00 37.1	52623.6	2002 Dec 15	46.0	224.9	17.17	1.17	67.5 ± 2.0	Y
F9-7731.....	02 39 08.9	−35 07 10.7	52623.6	2002 Dec 15	40.0	167.2	17.09	1.51	48.5 ± 1.7	Y
F9-8025.....	02 39 02.3	−35 09 13.6	52623.6	2002 Dec 15	42.3	166.0	17.22	1.41	69.2 ± 1.9	Y
CPD −35 919.....	02 39 35.2	−34 30 37.0	48955.6	1992 Nov 29	4.3	125.1	17.22	1.41	4.6 ± 0.7	N ^{v,p}
	02 39 35.2	−34 30 37.0	48956.5	1992 Nov 30	4.3	125.1	17.22	1.41	5.1 ± 0.7	N ^{v,p}
	02 39 35.2	−34 30 37.0	48957.6	1992 Dec 01	4.3	125.1	17.22	1.41	2.8 ± 0.8	N ^{v,p}
	02 39 35.2	−34 30 37.0	48958.6	1992 Dec 02	4.3	125.1	17.22	1.41	3.5 ± 0.8	N ^{v,p}
	02 39 35.2	−34 30 37.0	48959.6	1992 Dec 03	4.3	125.1	17.22	1.41	3.4 ± 0.7	N ^{v,p}
	02 39 35.2	−34 30 37.0	48961.6	1992 Dec 05	4.3	125.1	17.22	1.41	4.6 ± 0.8	N ^{v,p}
	02 39 35.2	−34 30 37.0	48962.6	1992 Dec 06	4.3	125.1	17.22	1.41	5.0 ± 0.8	N ^{v,p}
	02 39 35.2	−34 30 37.0	48963.6	1992 Dec 07	4.3	125.1	17.22	1.41	4.5 ± 0.8	N ^{v,p}
	02 39 35.2	−34 30 37.0	49333.6	1993 Dec 12	4.3	125.1	17.22	1.41	3.8 ± 0.7	N ^{v,p}
	02 39 35.2	−34 30 37.0	49333.8	1993 Dec 12	4.3	125.1	17.22	1.41	3.7 ± 0.8	N ^{v,p}
	02 39 35.2	−34 30 37.0	49334.5	1993 Dec 13	4.3	125.1	17.22	1.41	3.1 ± 0.8	N ^{v,p}
	02 39 35.2	−34 30 37.0	49334.8	1993 Dec 13	4.3	125.1	17.22	1.41	3.8 ± 0.8	N ^{v,p}
	02 39 35.2	−34 30 37.0	49335.5	1993 Dec 14	4.3	125.1	17.22	1.41	3.4 ± 0.8	N ^{v,p}
	02 39 35.2	−34 30 37.0	49335.8	1993 Dec 14	4.3	125.1	17.22	1.41	6.4 ± 0.9	N ^{v,p}
	02 39 35.2	−34 30 37.0	49336.7	1993 Dec 15	4.3	125.1	17.22	1.41	3.2 ± 0.7	N ^{v,p}
	02 39 35.2	−34 30 37.0	49337.5	1993 Dec 16	4.3	125.1	17.22	1.41	3.9 ± 0.7	N ^{v,p}
	02 39 35.2	−34 30 37.0	49337.8	1993 Dec 16	4.3	125.1	17.22	1.41	3.7 ± 0.7	N ^{v,p}
	02 39 35.2	−34 30 37.0	49338.5	1993 Dec 17	4.3	125.1	17.22	1.41	1.9 ± 0.7	N ^{v,p}
	02 39 35.2	−34 30 37.0	49339.5	1993 Dec 18	4.3	125.1	17.22	1.41	6.0 ± 0.7	N ^{v,p}
	02 39 35.2	−34 30 37.0	49339.8	1993 Dec 18	4.3	125.1	17.22	1.41	4.8 ± 0.7	N ^{v,p}
	02 39 35.2	−34 30 37.0	49340.5	1993 Dec 19	4.3	125.1	17.22	1.41	5.3 ± 0.7	N ^{v,p}
	02 39 35.2	−34 30 37.0	49340.8	1993 Dec 19	4.3	125.1	17.22	1.41	4.1 ± 0.7	N ^{v,p}
	02 39 35.2	−34 30 37.0	49341.5	1993 Dec 20	4.3	125.1	17.22	1.41	3.2 ± 0.6	N ^{v,p}
	02 39 35.2	−34 30 37.0	49341.8	1993 Dec 20	4.3	125.1	17.22	1.41	4.0 ± 0.7	N ^{v,p}
	02 39 35.2	−34 30 37.0	49648.5	1994 Oct 22	4.3	125.1	17.22	1.41	3.7 ± 0.7	N ^{v,p}
	02 39 35.2	−34 30 37.0	49649.5	1994 Oct 23	4.3	125.1	17.22	1.41	4.2 ± 0.7	N ^{v,p}
	02 39 35.2	−34 30 37.0	49650.5	1994 Oct 24	4.3	125.1	17.22	1.41	3.9 ± 0.7	N ^{v,p}
	02 39 35.2	−34 30 37.0	49651.5	1994 Oct 25	4.3	125.1	17.22	1.41	4.4 ± 0.8	N ^{v,p}
	02 39 35.2	−34 30 37.0	49652.5	1994 Oct 26	4.3	125.1	17.22	1.41	4.0 ± 0.8	N ^{v,p}
	02 39 35.2	−34 30 37.0	49652.9	1994 Oct 26	4.3	125.1	17.22	1.41	3.6 ± 0.8	N ^{v,p}
	02 39 35.2	−34 30 37.0	49653.5	1994 Oct 27	4.3	125.1	17.22	1.41	4.9 ± 0.8	N ^{v,p}
	02 39 35.2	−34 30 37.0	49653.8	1994 Oct 27	4.3	125.1	17.22	1.41	3.7 ± 0.9	N ^{v,p}

NOTES.—Units of right ascension are hours, minutes, and seconds, and units of declination are degrees, arcminutes, and arcseconds. Table 1 is also available in machine-readable form in the electronic edition of the *Astronomical Journal*.

the HRF radial velocities (see D. N. C. Lin & S. Dong 2006, in preparation). A nonrotating object might thereby give the appearance of rotation to the HRF observer, and a truly rotating object may appear to rotate at a different speed and/or about a different axis. In order to test for Fornax rotation, we correct for this perspective effect by placing our HRF radial velocity data set in the GRF.

Let \mathbf{v}_* be the GRF space velocity of a given Fornax star; we seek to determine the component of \mathbf{v}_* along the line of sight from the Sun to the star. Let \mathbf{v}_\odot be the velocity of the Sun with respect to the LSR, and let \mathbf{v}_F be the bulk velocity of Fornax with respect to the LSR. Then the projection of the relative motion between the Sun and Fornax along the line of sight to the given star is the sum of scalar products:

$$v_{\text{rel}}(l, b) = \frac{\mathbf{v}_*}{|\mathbf{v}_*|} \cdot (\mathbf{v}_\odot - \mathbf{v}_F). \quad (6)$$

We apply equations (5) and (6) along the line of sight to every star in the Fornax velocity data set in order to determine each

star's GRF radial velocity. For each star's GRF radial velocity uncertainty we adopt the corresponding measurement uncertainty originally estimated in § 2.3. We adopt the value $v_\odot = 13.7 \text{ km s}^{-1}$ toward $(l, b) = (26^\circ 6', 31^\circ 4')$ (Dehnen & Binney 1998). The three components of Fornax's velocity with respect to the LSR are computed from Fornax's heliocentric radial velocity and proper motion, via equations (44)–(46) of Piatek et al. (2002). We adopt $+53.3 \text{ km s}^{-1}$ as the heliocentric radial velocity of Fornax. Piatek et al. (2002) and Dinescu et al. (2004) provide independent measurements of the Fornax proper motion. Since their results agree only at the $\sim 2 \sigma$ level, we consider both cases independently, giving two possible GRF radial velocity data sets.

We then test the two resulting GRF radial velocity data sets for rotation. In both cases we consider the position angle of every star in the intermediate $N = 182$ member sample to coincide with that of a prospective rotation axis. For each star we bisect the face of Fornax with a line having that star's position angle and then calculate the mean GRF radial velocity from the member stars on either side of the line. Figure 4 plots the hemispheric mean

TABLE 2
RESULTS FOR RADIAL VELOCITY STANDARD STARS

Star	$\alpha_{J2000.0}$	$\delta_{J2000.0}$	$v_{\text{published}}^a$ (km s^{-1})	HJD (-2,400,000.0)	UT Date of Observation	v (km s^{-1})	$\langle v \rangle^b$ (km s^{-1})	
HD 196983	20 41 50.5	-33 53 16.9	-9.1 ± 0.3^c	48954.5	1992 Nov 28	-9.0 ± 0.6	-9.3 ± 0.9	
	20 41 50.5	-33 53 16.9	-9.1 ± 0.3^c	48955.5	1992 Nov 29	-9.3 ± 0.7	-9.3 ± 0.9	
	20 41 50.5	-33 53 16.9	-9.1 ± 0.3^c	48956.5	1992 Nov 30	-8.1 ± 0.6	-9.3 ± 0.9	
	20 41 50.5	-33 53 16.9	-9.1 ± 0.3^c	48957.5	1992 Dec 01	-10.1 ± 0.8	-9.3 ± 0.9	
	20 41 50.5	-33 53 16.9	-9.1 ± 0.3^c	48958.5	1992 Dec 02	-10.3 ± 0.8	-9.3 ± 0.9	
	20 41 50.5	-33 53 16.9	-9.1 ± 0.3^c	48959.5	1992 Dec 03	-9.9 ± 0.8	-9.3 ± 0.9	
	20 41 50.5	-33 53 16.9	-9.1 ± 0.3^c	48960.5	1992 Dec 04	-9.2 ± 0.8	-9.3 ± 0.9	
	20 41 50.5	-33 53 16.9	-9.1 ± 0.3^c	48961.5	1992 Dec 05	-9.9 ± 0.8	-9.3 ± 0.9	
	20 41 50.5	-33 53 16.9	-9.1 ± 0.3^c	48962.5	1992 Dec 06	-9.8 ± 0.8	-9.3 ± 0.9	
	20 41 50.5	-33 53 16.9	-9.1 ± 0.3^c	48963.5	1992 Dec 07	-9.8 ± 0.7	-9.3 ± 0.9	
	20 41 50.5	-33 53 16.9	-9.1 ± 0.3^c	49648.5	1994 Oct 22	-9.9 ± 0.7	-9.3 ± 0.9	
	20 41 50.5	-33 53 16.9	-9.1 ± 0.3^c	49649.5	1994 Oct 23	-8.7 ± 0.7	-9.3 ± 0.9	
	20 41 50.5	-33 53 16.9	-9.1 ± 0.3^c	49650.5	1994 Oct 24	-8.6 ± 0.7	-9.3 ± 0.9	
	20 41 50.5	-33 53 16.9	-9.1 ± 0.3^c	49651.5	1994 Oct 25	-8.3 ± 0.8	-9.3 ± 0.9	
	20 41 50.5	-33 53 16.9	-9.1 ± 0.3^c	49652.5	1994 Oct 26	-9.4 ± 0.8	-9.3 ± 0.9	
	20 41 50.5	-33 53 16.9	-9.1 ± 0.3^c	49653.5	1994 Oct 27	-9.1 ± 0.7	-9.3 ± 0.9	
	HD 219509	23 17 17.6	-66 54 48.4	$+67.5 \pm 0.5^c$	48954.5	1992 Nov 28	67.9 ± 0.8	$+67.8 \pm 1.0$
		23 17 17.6	-66 54 48.4	$+67.5 \pm 0.5^c$	48955.5	1992 Nov 29	67.0 ± 0.8	$+67.8 \pm 1.0$
		23 17 17.6	-66 54 48.4	$+67.5 \pm 0.5^c$	48956.5	1992 Nov 30	70.0 ± 0.8	$+67.8 \pm 1.0$
		23 17 17.6	-66 54 48.4	$+67.5 \pm 0.5^c$	48957.5	1992 Dec 01	68.5 ± 0.9	$+67.8 \pm 1.0$
23 17 17.6		-66 54 48.4	$+67.5 \pm 0.5^c$	48958.5	1992 Dec 02	67.0 ± 0.9	$+67.8 \pm 1.0$	
23 17 17.6		-66 54 48.4	$+67.5 \pm 0.5^c$	48959.5	1992 Dec 03	68.6 ± 0.9	$+67.8 \pm 1.0$	
23 17 17.6		-66 54 48.4	$+67.5 \pm 0.5^c$	48960.5	1992 Dec 04	68.3 ± 0.9	$+67.8 \pm 1.0$	
23 17 17.6		-66 54 48.4	$+67.5 \pm 0.5^c$	48961.5	1992 Dec 05	67.1 ± 0.9	$+67.8 \pm 1.0$	
23 17 17.6		-66 54 48.4	$+67.5 \pm 0.5^c$	48962.5	1992 Dec 06	67.8 ± 0.9	$+67.8 \pm 1.0$	
23 17 17.6		-66 54 48.4	$+67.5 \pm 0.5^c$	48963.5	1992 Dec 07	68.5 ± 0.9	$+67.8 \pm 1.0$	
23 17 17.6		-66 54 48.4	$+67.5 \pm 0.5^c$	49333.5	1993 Dec 12	66.6 ± 0.9	$+67.8 \pm 1.0$	
23 17 17.6		-66 54 48.4	$+67.5 \pm 0.5^c$	49335.5	1993 Dec 14	68.1 ± 1.0	$+67.8 \pm 1.0$	
23 17 17.6		-66 54 48.4	$+67.5 \pm 0.5^c$	49337.5	1993 Dec 16	67.2 ± 0.8	$+67.8 \pm 1.0$	
23 17 17.6		-66 54 48.4	$+67.5 \pm 0.5^c$	49338.5	1993 Dec 17	68.0 ± 0.8	$+67.8 \pm 1.0$	
23 17 17.6		-66 54 48.4	$+67.5 \pm 0.5^c$	49339.5	1993 Dec 18	68.2 ± 0.9	$+67.8 \pm 1.0$	
23 17 17.6		-66 54 48.4	$+67.5 \pm 0.5^c$	49340.5	1993 Dec 19	66.7 ± 0.8	$+67.8 \pm 1.0$	
23 17 17.6		-66 54 48.4	$+67.5 \pm 0.5^c$	49341.5	1993 Dec 20	67.9 ± 0.8	$+67.8 \pm 1.0$	
23 17 17.6		-66 54 48.4	$+67.5 \pm 0.5^c$	49648.5	1994 Oct 22	66.1 ± 0.9	$+67.8 \pm 1.0$	
23 17 17.6		-66 54 48.4	$+67.5 \pm 0.5^c$	49649.5	1994 Oct 23	67.9 ± 0.8	$+67.8 \pm 1.0$	
23 17 17.6		-66 54 48.4	$+67.5 \pm 0.5^c$	49650.5	1994 Oct 24	68.2 ± 0.8	$+67.8 \pm 1.0$	
23 17 17.6	-66 54 48.4	$+67.5 \pm 0.5^c$	49651.5	1994 Oct 25	67.6 ± 0.9	$+67.8 \pm 1.0$		
23 17 17.6	-66 54 48.4	$+67.5 \pm 0.5^c$	49652.5	1994 Oct 26	68.0 ± 0.9	$+67.8 \pm 1.0$		
CPD -43 2527	06 32 15.3	-43 31 14.3	$+19.7 \pm 0.9^c$	48954.9	1992 Nov 28	19.7 ± 0.7	$+19.8 \pm 0.9$	
	06 32 15.3	-43 31 14.3	$+19.7 \pm 0.9^c$	48955.9	1992 Nov 29	20.4 ± 0.7	$+19.8 \pm 0.9$	
	06 32 15.3	-43 31 14.3	$+19.7 \pm 0.9^c$	48957.8	1992 Dec 01	19.8 ± 0.8	$+19.8 \pm 0.9$	
	06 32 15.3	-43 31 14.3	$+19.7 \pm 0.9^c$	48958.9	1992 Dec 02	20.1 ± 0.8	$+19.8 \pm 0.9$	
	06 32 15.3	-43 31 14.3	$+19.7 \pm 0.9^c$	48959.9	1992 Dec 03	20.2 ± 0.8	$+19.8 \pm 0.9$	
	06 32 15.3	-43 31 14.3	$+19.7 \pm 0.9^c$	48960.9	1992 Dec 04	18.1 ± 0.8	$+19.8 \pm 0.9$	
	06 32 15.3	-43 31 14.3	$+19.7 \pm 0.9^c$	48961.9	1992 Dec 05	20.0 ± 0.9	$+19.8 \pm 0.9$	
	06 32 15.3	-43 31 14.3	$+19.7 \pm 0.9^c$	48962.9	1992 Dec 06	20.0 ± 0.8	$+19.8 \pm 0.9$	
	06 32 15.3	-43 31 14.3	$+19.7 \pm 0.9^c$	48963.9	1992 Dec 07	20.0 ± 0.8	$+19.8 \pm 0.9$	
	06 32 15.3	-43 31 14.3	$+19.7 \pm 0.9^c$	49333.8	1993 Dec 12	19.7 ± 0.8	$+19.8 \pm 0.9$	
	06 32 15.3	-43 31 14.3	$+19.7 \pm 0.9^c$	49334.9	1993 Dec 13	20.0 ± 0.8	$+19.8 \pm 0.9$	
	06 32 15.3	-43 31 14.3	$+19.7 \pm 0.9^c$	49335.9	1993 Dec 14	22.1 ± 0.9	$+19.8 \pm 0.9$	
	06 32 15.3	-43 31 14.3	$+19.7 \pm 0.9^c$	49335.9	1993 Dec 14	20.0 ± 0.7	$+19.8 \pm 0.9$	
	06 32 15.3	-43 31 14.3	$+19.7 \pm 0.9^c$	49336.9	1993 Dec 15	18.7 ± 0.7	$+19.8 \pm 0.9$	
	06 32 15.3	-43 31 14.3	$+19.7 \pm 0.9^c$	49338.9	1993 Dec 17	20.0 ± 0.7	$+19.8 \pm 0.9$	
	06 32 15.3	-43 31 14.3	$+19.7 \pm 0.9^c$	49339.9	1993 Dec 18	19.4 ± 0.7	$+19.8 \pm 0.9$	
	06 32 15.3	-43 31 14.3	$+19.7 \pm 0.9^c$	49340.9	1993 Dec 19	20.4 ± 0.7	$+19.8 \pm 0.9$	
	06 32 15.3	-43 31 14.3	$+19.7 \pm 0.9^c$	49341.9	1993 Dec 20	20.4 ± 0.8	$+19.8 \pm 0.9$	
	06 32 15.3	-43 31 14.3	$+19.7 \pm 0.9^c$	49648.9	1994 Oct 22	19.7 ± 0.7	$+19.8 \pm 0.9$	
	06 32 15.3	-43 31 14.3	$+19.7 \pm 0.9^c$	49649.9	1994 Oct 23	19.7 ± 0.7	$+19.8 \pm 0.9$	
06 32 15.3	-43 31 14.3	$+19.7 \pm 0.9^c$	49650.9	1994 Oct 24	20.6 ± 0.7	$+19.8 \pm 0.9$		
06 32 15.3	-43 31 14.3	$+19.7 \pm 0.9^c$	49651.9	1994 Oct 25	19.1 ± 0.8	$+19.8 \pm 0.9$		
06 32 15.3	-43 31 14.3	$+19.7 \pm 0.9^c$	49652.9	1994 Oct 26	18.7 ± 0.9	$+19.8 \pm 0.9$		
06 32 15.3	-43 31 14.3	$+19.7 \pm 0.9^c$	49653.9	1994 Oct 27	18.9 ± 0.8	$+19.8 \pm 0.9$		

TABLE 2—Continued

Star	$\alpha_{J2000.0}$	$\delta_{J2000.0}$	$v_{\text{published}}^a$ (km s^{-1})	HJD ($-2,400,000.0$)	UT Date of Observation	v (km s^{-1})	$\langle v \rangle^b$ (km s^{-1})
HD 23214	03 42 09.1	-34 25 14.8	-4.3 ± 1.8^d	49333.6	1993 Dec 12	-4.9 ± 0.7	-5.1 ± 0.9
	03 42 09.1	-34 25 14.8	-4.3 ± 1.8^d	49334.5	1993 Dec 13	-5.3 ± 0.7	-5.1 ± 0.9
	03 42 09.1	-34 25 14.8	-4.3 ± 1.8^d	49336.8	1993 Dec 15	-5.3 ± 0.7	-5.1 ± 0.9
	03 42 09.1	-34 25 14.8	-4.3 ± 1.8^d	49648.9	1994 Oct 22	-5.0 ± 0.8	-5.1 ± 0.9
HD 43880	06 17 06.3	-34 44 13.1	$+43.6 \pm 2.4^d$	49333.8	1993 Dec 12	45.3 ± 0.8	$+46.3 \pm 0.9$
	06 17 06.3	-34 44 13.1	$+43.6 \pm 2.4^d$	49334.8	1993 Dec 13	47.9 ± 0.8	$+46.3 \pm 0.9$
	06 17 06.3	-34 44 13.1	$+43.6 \pm 2.4^d$	49335.8	1993 Dec 14	47.4 ± 0.8	$+46.3 \pm 0.9$
	06 17 06.3	-34 44 13.1	$+43.6 \pm 2.4^d$	49336.8	1993 Dec 15	45.1 ± 0.7	$+46.3 \pm 0.9$
	06 17 06.3	-34 44 13.1	$+43.6 \pm 2.4^d$	49337.9	1993 Dec 16	45.9 ± 0.7	$+46.3 \pm 0.9$
	06 17 06.3	-34 44 13.1	$+43.6 \pm 2.4^d$	49338.8	1993 Dec 17	47.4 ± 0.6	$+46.3 \pm 0.9$
	06 17 06.3	-34 44 13.1	$+43.6 \pm 2.4^d$	49339.9	1993 Dec 18	46.0 ± 0.7	$+46.3 \pm 0.9$
	06 17 06.3	-34 44 13.1	$+43.6 \pm 2.4^d$	49340.9	1993 Dec 19	45.9 ± 0.7	$+46.3 \pm 0.9$
	06 17 06.3	-34 44 13.1	$+43.6 \pm 2.4^d$	49341.9	1993 Dec 20	45.8 ± 0.7	$+46.3 \pm 0.9$
	Twilight sky	49333.9	1993 Dec 12	-1.4 ± 1.4
...	49334.5	1993 Dec 13	-0.6 ± 1.0	-0.2 ± 1.2
...	49335.5	1993 Dec 14	0.7 ± 1.1	-0.2 ± 1.2
...	49335.5	1993 Dec 14	0.2 ± 1.0	-0.2 ± 1.2
...	49337.5	1993 Dec 16	-0.8 ± 1.0	-0.2 ± 1.2
...	49338.5	1993 Dec 17	-0.3 ± 1.0	-0.2 ± 1.2
...	49339.5	1993 Dec 18	-0.3 ± 1.0	-0.2 ± 1.2
...	49341.5	1993 Dec 20	0.0 ± 1.0	-0.2 ± 1.2
HD 6655	01 05 18.0	-72 33 21.0	$+19.5 \pm 0.3^c$	52620.5	2002 Dec 12	18.8 ± 0.7	$+19.2 \pm 1.1$
	01 05 18.0	-72 33 21.0	$+19.5 \pm 0.3^c$	52620.5	2002 Dec 12	18.9 ± 0.7	$+19.2 \pm 1.1$
	01 05 18.0	-72 33 21.0	$+19.5 \pm 0.3^c$	52621.5	2002 Dec 13	20.0 ± 0.7	$+19.2 \pm 1.1$
	01 05 18.0	-72 33 21.0	$+19.5 \pm 0.3^c$	52622.5	2002 Dec 14	19.4 ± 0.7	$+19.2 \pm 1.1$
HD 21581	03 28 54.8	-00 25 03.1	$+154 \pm 1^e$	52620.6	2002 Dec 12	152.1 ± 0.8	$+151.3 \pm 1.3$
	03 28 54.8	-00 25 03.1	$+154 \pm 1^e$	52621.6	2002 Dec 13	150.6 ± 0.9	$+151.3 \pm 1.3$
SAO 217998	06 32 15.6	-43 31 13.4	$+13.1^f$	52620.6	2002 Dec 12	18.9 ± 0.5	$+19.0 \pm 1.6$
	06 32 15.6	-43 31 13.4	$+13.1^f$	52621.6	2002 Dec 13	18.4 ± 0.7	$+19.0 \pm 1.6$
	06 32 15.6	-43 31 13.4	$+13.1^f$	52621.8	2002 Dec 13	19.6 ± 0.5	$+19.0 \pm 1.6$
	06 32 15.6	-43 31 13.4	$+13.1^f$	52622.6	2002 Dec 14	19.1 ± 0.5	$+19.0 \pm 1.6$
	06 32 15.6	-43 31 13.4	$+13.1^f$	52622.8	2002 Dec 14	17.8 ± 0.6	$+19.0 \pm 1.6$
	06 32 15.6	-43 31 13.4	$+13.1^f$	52623.5	2002 Dec 15	20.1 ± 0.6	$+19.0 \pm 1.6$
	06 32 15.6	-43 31 13.4	$+13.1^f$	52623.6	2002 Dec 15	18.0 ± 0.6	$+19.0 \pm 1.6$
	06 32 15.6	-43 31 13.4	$+13.1^f$	52623.6	2002 Dec 15	20.2 ± 0.6	$+19.0 \pm 1.6$
	06 32 15.6	-43 31 13.4	$+13.1^f$	52623.8	2002 Dec 15	19.4 ± 0.6	$+19.0 \pm 1.6$
	06 32 15.6	-43 31 13.4	$+13.1^f$	52623.8	2002 Dec 15	19.4 ± 0.6	$+19.0 \pm 1.6$
HD 83516	09 38 02.9	-35 04 34.0	$+43.5 \pm 0.2^c$	52620.9	2002 Dec 12	43.2 ± 0.4	$+42.6 \pm 0.7$
	09 38 02.9	-35 04 34.0	$+43.5 \pm 0.2^c$	52621.8	2002 Dec 13	42.4 ± 0.4	$+42.6 \pm 0.7$
	09 38 02.9	-35 04 34.0	$+43.5 \pm 0.2^c$	52622.9	2002 Dec 14	42.9 ± 0.5	$+42.6 \pm 0.7$
	09 38 02.9	-35 04 34.0	$+43.5 \pm 0.2^c$	52622.9	2002 Dec 14	42.6 ± 0.4	$+42.6 \pm 0.7$
	09 38 02.9	-35 04 34.0	$+43.5 \pm 0.2^c$	52622.9	2002 Dec 14	43.9 ± 0.6	$+42.6 \pm 0.7$
	09 38 02.9	-35 04 34.0	$+43.5 \pm 0.2^c$	52623.8	2002 Dec 15	40.2 ± 0.6	$+42.6 \pm 0.7$
	09 38 02.9	-35 04 34.0	$+43.5 \pm 0.2^c$	52621.8	2002 Dec 13	40.2 ± 0.5	$+40.2 \pm 0.9$
	09 38 02.9	-35 04 34.0	$+43.5 \pm 0.2^c$	52623.8	2002 Dec 15	40.3 ± 0.6	$+40.2 \pm 0.9$
SAO 201636	10 41 09.5	-30 47 05.8	$+262 \pm 1^e$	52621.8	2002 Dec 13	264.3 ± 0.9	$+264.3 \pm 1.4$
HD 2796	00 31 16.5	-16 47 43.6	-61 ± 1^e	52623.5	2002 Dec 15	-64.5 ± 1.0	-54.5 ± 1.5
HD 103545	11 55 26.2	09 07 54.4	$+180 \pm 1^e$	52623.9	2002 Dec 15	177.0 ± 1.0	$+177.0 \pm 1.5$

NOTE.—Table 2 is also available in machine-readable form in the electronic edition of the *Astronomical Journal*.

^a Published radial velocity.

^b Weighted mean measured radial velocity from the results presented in this table.

^c CORAVEL study (Udry et al. 1999).

^d Olszewski et al. (1991).

^e Beers et al. (2000).

^f Evans (1967).

velocity *difference* as a function of the bisecting line's position angle. Figures 4b and 4c depict the GRF rotation signal assuming the Piatek et al. (2002) and Dinescu et al. (2004) proper motions, respectively. For comparison, Figure 4a shows the HRF apparent rotation signal, uncorrected for any perspective-induced velocity gradient. The half-amplitude of the sinusoid fit in each plot measures a characteristic rotation speed, whereas the sinusoid's phase indicates the orientation of the rotation axis. We summarize the results of this test in Table 5. Columns (4) and (5) of Table 5 list the

characteristic rotation speed and orientation of the rotation axis, respectively. The uncertainties given for these values reflect the range of values obtained using all proper motions allowed within the published (1σ) proper-motion uncertainties. Uncertainties in the solar motion and in the HRF radial velocities of the Fornax stars are not considered here. To assess the significance of a rotation detection, we performed Monte Carlo simulations in which 10^4 samples of 182 stars having positions of those in the actual sample were drawn at random from a nonrotating, Gaussian

TABLE 3
REPEAT VELOCITY MEASUREMENTS

Star	$\langle v \rangle$ (km s ⁻¹)	χ^{2a}	$p(\chi^2)^b$	N
CPD -43 2527.....	19.8 ± 0.8	21.8	0.5327	24
Twilight Sky.....	-0.2 ± 1.0	1.3	0.9722	7
F1-4.....	43.7 ± 1.8	0.2	0.9204	3
F1-2.....	44.2 ± 2.4	0.4	0.5105	2
F1-1.....	61.4 ± 2.3	6.6	0.0103	2
CPD -35 919.....	4.1 ± 0.7	47.6	0.0288	32
F-M17.....	85.6 ± 2.4	0.1	0.9364	3
F-M26.....	42.0 ± 2.2	1.2	0.2813	3
F-M4.....	52.7 ± 2.2	0.1	0.7369	2
F-M6.....	34.0 ± 2.2	3.1	0.0785	2
F-M8.....	53.8 ± 2.5	2.6	0.1101	2
F10-1.....	53.7 ± 2.4	0.3	0.6086	2
F15-4.....	54.8 ± 1.9	0.4	0.5157	2
F17-4.....	49.5 ± 2.6	7.3	0.0069	2
F19-5.....	46.9 ± 2.8	4.7	0.0295	2
F2-1.....	50.4 ± 2.4	0.0	0.8516	2
F2-9.....	50.9 ± 2.1	21.4	0.0000	2
F24-2.....	17.7 ± 2.5	2.5	0.1137	2
F3-5.....	55.4 ± 2.6	0.1	0.7647	2
F31-3.....	5.9 ± 2.6	3.2	0.2063	3
F9-6.....	70.7 ± 2.5	1.9	0.1734	2
HD 196983.....	-9.3 ± 0.7	12.7	0.6242	16
HD 21581.....	151.3 ± 0.8	1.5	0.2151	2
HD 219509.....	67.8 ± 0.9	22.2	0.3862	22
HD 23214.....	-5.1 ± 0.7	0.3	0.9608	4
HD 43880.....	46.3 ± 0.7	14.6	0.0685	9
HD 48381.....	40.2 ± 0.5	0.0	0.8648	2
HD 6655.....	19.2 ± 0.7	1.9	0.5916	4
HD 83516.....	42.6 ± 0.5	23.6	0.0003	6
SAO 217998.....	19.0 ± 1.0	17.0	0.0306	9

^a Parameter $\chi^2 = \sum_{i=1}^N [(v_i - \langle v \rangle)^2 / \sigma_i^2]$.

^b Probability that χ^2 would have at least the measured value, given N independent measurements having the estimated uncertainties.

velocity distribution with $\sigma = 12.4$ km s⁻¹. Column (6) of Table 5 gives the percentage of these artificial samples for which we would measure a rotation speed greater than the observed speed listed in column (4). A lower percentage indicates a more statistically significant observed rotation.

We find that although both published proper-motion measurements imply Fornax rotation about an axis at position angle $\sim 115^\circ$, only the rotation detected using the Piatek et al. (2002) proper motion is (marginally) statistically significant. Fewer than 10% of Monte Carlo trials produce rotation as fast as the ~ 2.5 km s⁻¹ implied by the Piatek et al. (2002) proper motion. Nearly three in four trials produce the ~ 1.2 km s⁻¹ rotation implied by the Dinescu et al. (2004) proper motion. Therefore, due to perspective effects and the existing uncertainty in the proper motion, we cannot state definitively how or even if Fornax rotates. If we simply *assume* that Fornax does not rotate, we can use the apparent rotation seen in the HRF radial velocity data indirectly to “measure” Fornax’s proper motion. The uncorrected HRF data indicate ~ 2.0 km s⁻¹ “rotation” about an axis at $\sim 140^\circ$. A Fornax GRF proper motion of $(\mu_l, \mu_b) = (-52 \text{ mas century}^{-1}, +41 \text{ mas century}^{-1})$, when applied to these data, would produce a GRF radial velocity data set showing zero rotation (Fig. 4d).

These results and Fornax’s velocity dispersion of >10 km s⁻¹ (§ 3.4) indicate that, aside from a possible tidal interpretation (§ 4.3), any real rotational component is dynamically insignifi-

TABLE 4
COMPARISON WITH PREVIOUSLY MEASURED VELOCITIES

Star	UT Date of Observation	v (km s ⁻¹)	$\langle v \rangle$ (km s ⁻¹)	χ^2	$p(\chi^2)$
F-M1.....	1989 Nov 30	56.7 ± 2.9	55.1 ± 2.6	2.0	0.368
	1994 Oct 23	51.8 ± 2.8	55.1 ± 2.6	2.0	0.368
F-M10.....	1989 Dec 03	65.1 ± 1.3	63.1 ± 1.6	5.8	0.0562
	1990 Nov 17	63.8 ± 1.8	63.1 ± 1.6	5.8	0.0562
	1993 Dec 18	56.5 ± 2.2	63.1 ± 1.6	5.8	0.0562
F-M13.....	1989 Dec 03	92.1 ± 2.0	90.9 ± 2.1	0.9	0.3414
	1994 Oct 25	89.2 ± 2.3	90.9 ± 2.1	0.9	0.3414
F-M15.....	1989 Dec 04	57.9 ± 2.0	60.0 ± 1.9	2.0	0.1579
	1993 Dec 12	61.7 ± 1.8	60.0 ± 1.9	2.0	0.1579
F-M17.....	1989 Dec 05	87.8 ± 1.9	86.5 ± 2.2	0.2	0.9931
	1990 Nov 14	86.7 ± 2.2	86.5 ± 2.2	0.2	0.9931
	1993 Dec 17	85.1 ± 2.4	86.5 ± 2.2	0.2	0.9931
	1994 Oct 25	86.3 ± 2.4	86.5 ± 2.2	0.2	0.9931
	1994 Oct 26	85.5 ± 2.5	86.5 ± 2.2	0.2	0.9931
F-M2.....	1989 Dec 01	71.6 ± 1.5	71.6 ± 1.8	0.0	0.9469
	1993 Dec 14	71.8 ± 2.6	71.6 ± 1.8	0.0	0.9469
F-M20.....	1990 Nov 15	38.9 ± 2.0	49.6 ± 2.1	66.2	0.0000
	1993 Dec 13	63.7 ± 2.3	49.6 ± 2.1	66.2	0.0000
F-M26.....	1990 Nov 18	40.3 ± 1.6	41.4 ± 1.9	1.1	0.5906
	1993 Dec 20	43.8 ± 2.0	41.4 ± 1.9	1.1	0.5906
	1994 Oct 23	40.3 ± 2.5	41.4 ± 1.9	1.1	0.5906
F-M3.....	1990 Dec 01	59.1 ± 2.8	58.2 ± 2.1	0.2	0.6961
	1994 Oct 24	57.8 ± 1.8	58.2 ± 2.1	0.2	0.6961
F-M4.....	1989 Dec 01	60.0 ± 3.6	53.6 ± 2.3	1.2	0.7451
	1990 Nov 15	52.9 ± 2.1	53.6 ± 2.3	1.2	0.7451
	1993 Dec 12	52.3 ± 2.0	53.6 ± 2.3	1.2	0.7451
	1994 Oct 22	53.4 ± 2.6	53.6 ± 2.3	1.2	0.7451
F-M6.....	1989 Dec 02	34.9 ± 1.9	34.5 ± 2.2	1.1	0.7805
	1990 Nov 16	35.5 ± 2.9	34.5 ± 2.2	1.1	0.7805
	1993 Dec 18	31.9 ± 2.0	34.5 ± 2.2	1.1	0.7805
	1994 Oct 26	37.7 ± 2.7	34.5 ± 2.2	1.1	0.7805
F-M7.....	1989 Dec 02	42.3 ± 2.5	42.0 ± 2.7	0.0	0.8377
	1994 Oct 24	41.5 ± 3.0	42.0 ± 2.7	0.0	0.8377
F-M8.....	1989 Dec 02	54.4 ± 2.5	54.6 ± 2.5	1.2	0.7644
	1989 Dec 04	56.9 ± 2.7	54.6 ± 2.5	1.2	0.7644
	1993 Dec 19	51.4 ± 2.3	54.6 ± 2.5	1.2	0.7644
	1994 Oct 27	57.0 ± 2.7	54.6 ± 2.5	1.2	0.7644

NOTES.—Entries with UT date prior to 1992 were published in M91. All other entries are from the present study.

cant. Given the proper-motion ambiguity, we use the HRF radial velocity values of Table 1 in the velocity dispersion calculations that follow. We demonstrate in § 3.4 that velocity dispersions measured in the HRF differ negligibly from their plausible GRF values.

3.4. Velocity Dispersion

3.4.1. Maximum Likelihood

We use maximum likelihood statistics to estimate the mean heliocentric velocity and intrinsic velocity dispersion of those stars we have determined to be members. Let v_i , u_i , and σ_i now be the measured radial velocity, the true radial velocity, and the internal measurement uncertainty, respectively, for the i th of N stars. Then $v_i = u_i + \sigma_i \epsilon_i$, where the values $\{\epsilon_1, \dots, \epsilon_N\}$ have a standard normal probability distribution. There are two sources of variability in v_i : the random, internal measurement uncertainty, σ_i , and the intrinsic radial velocity dispersion, denoted σ_p , for the stars in the sample. The latter is the physical quantity of interest. If we assume that the values $\{v_1, \dots, v_N\}$ have a Gaussian distribution centered on the mean true velocity, denoted $\langle u \rangle$, then their

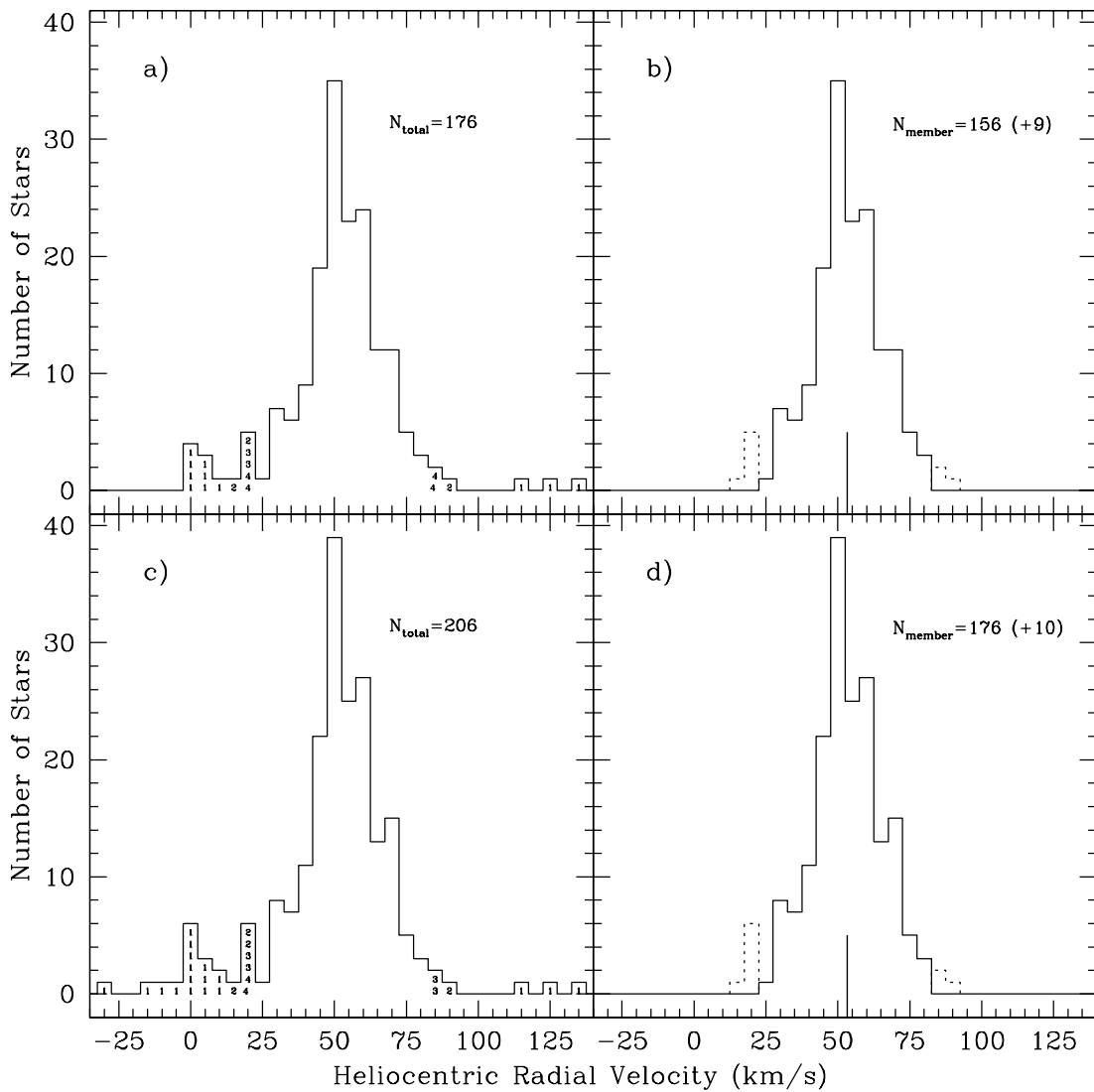


FIG. 3.—Heliocentric radial velocity distribution of four different groups of stars. (a) All 176 Fornax candidate member stars whose velocities are presented in Table 1. Stars that were later rejected by an iterative membership determination algorithm are numbered according to which iteration rejected them (e.g., “1”= first iteration). (b) The 156 stars determined to be probable Fornax members. (c) All 206 Fornax candidate member stars after combining our data with those of M91. Again, numbers specify which iteration removed probable nonmembers. (d) The 176 probable Fornax members from the combined data set. In (b) and (d), a thick vertical line marks the mean velocity of members calculated using maximum likelihood statistics. The regions enclosed by dotted lines in (b) and (d) represent those stars rejected in iterations 2, 3, and 4. We consider these to be borderline members.

joint probability function is the product of their individual Gaussian probabilities:

$$p(\{v_1, \dots, v_N\}) = \prod_{i=1}^N \frac{1}{\sqrt{2\pi(\sigma_i^2 + \sigma_p^2)}} \exp\left[-\frac{1}{2} \frac{(v_i - \langle u \rangle)^2}{(\sigma_i^2 + \sigma_p^2)}\right]. \quad (7)$$

Estimates of $\langle u \rangle$ and σ_p , denoted \hat{u} and $\hat{\sigma}_p$, are determined numerically as the values that maximize the natural logarithm of the probability function,

$$\ln(p) = -\frac{1}{2} \sum_{i=1}^N \ln(\sigma_i^2 + \sigma_p^2) - \frac{1}{2} \sum_{i=1}^N \frac{(v_i - \langle u \rangle)^2}{(\sigma_i^2 + \sigma_p^2)} - \frac{N}{2} \ln(2\pi). \quad (8)$$

As the logarithm is a monotonic function, this is equivalent to maximizing p itself (Rice 1995). To estimate confidence intervals for \hat{u} and $\hat{\sigma}_p$, we recognize that the Gaussian probability distributions for $(\hat{u} - \langle u \rangle)$ and $(\hat{\sigma}_p - \sigma_p)$ have centers at zero and a joint variability described by a covariance matrix. This covariance matrix, A , has elements

$$A = \begin{pmatrix} a & c \\ c & b \end{pmatrix}, \quad (9)$$

where diagonal elements a and b are the variances of $\langle u \rangle$ and σ_p , respectively. We determine a and b from the inverse of the covariance matrix, which has the property

$$A^{-1} = \begin{pmatrix} \frac{\partial^2 \ln(p)}{\partial \langle u \rangle^2} \Big|_{((\hat{u}), \hat{\sigma}_p)} & \frac{\partial^2 \ln(p)}{\partial \sigma_p \partial \langle u \rangle} \Big|_{((\hat{u}), \hat{\sigma}_p)} \\ \frac{\partial^2 \ln(p)}{\partial \langle u \rangle \partial \sigma_p} \Big|_{((\hat{u}), \hat{\sigma}_p)} & \frac{\partial^2 \ln(p)}{\partial \sigma_p^2} \Big|_{((\hat{u}), \hat{\sigma}_p)} \end{pmatrix}. \quad (10)$$

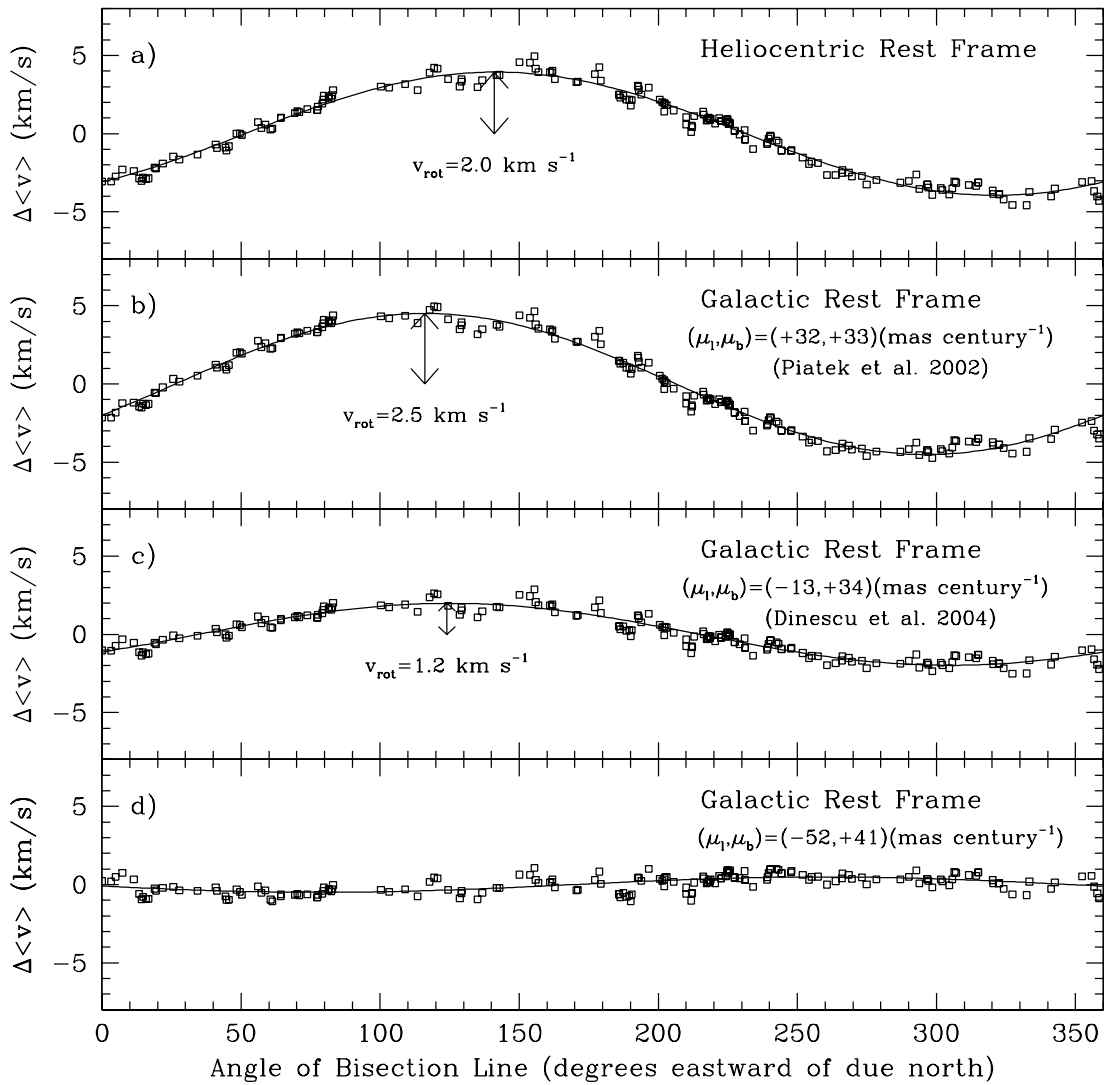


FIG. 4.—Rotation signal of Fornax. The difference between the radial velocity of Fornax members on either side of a line passing through Fornax’s center is plotted as a function of the position angle of that line. (a) Computed using the measured heliocentric rest-frame radial velocities, uncorrected for perspective-induced rotation (see § 3.3). (b) Computed from GRF radial velocities obtained using the Fornax proper-motion measurement of Piatek et al. (2002). (c) Computed from GRF radial velocities obtained using the Fornax proper-motion measurement of Dinescu et al. (2004). (d) Computed from GRF radial velocities obtained under the assumption that Fornax does not rotate.

Let $Z_{\alpha/2}$ denote the $\alpha/2$ quantile of the standard normal distribution. For confidence intervals containing the physical values $\langle u \rangle$ and σ_p with $100(1 - \alpha)\%$ probability, we report the mean velocity and velocity dispersion as $\langle \hat{u} \rangle \pm Z_{\alpha/2} \sqrt{a}$ and $\hat{\sigma}_p \pm Z_{\alpha/2} \sqrt{b}$, respectively. Conventional 68% confidence intervals are given by $\langle \hat{u} \rangle \pm \sqrt{a}$ and $\hat{\sigma}_p \pm \sqrt{b}$.

We estimate the mean true velocity and intrinsic velocity dispersion along the line of sight for three successively less stringent

levels of membership discrimination. In case *a* we consider as Fornax members only the $N = 176$ stars surviving all four iterations of the velocity rejection algorithm; in case *b* we reinstate the six stars rejected by iterations 3 and 4; and in case *c* we further add the four stars rejected by iteration 2. With 68% confidence intervals about the $(\langle \hat{u} \rangle, \hat{\sigma}_p)$ pairs in units of km s^{-1} , case *a* gives global values $(53.3 \pm 0.8, 11.1 \pm 0.6)$; case *b* gives $(53.0 \pm 0.9, 12.4 \pm 0.8)$; and case *c* gives $(52.6 \pm 1.0, 13.3 \pm 0.8)$.

TABLE 5
ROTATION SIGNALS IN THE GALACTIC REST FRAME

SOURCE (1)	PROPER MOTION		GRF ROTATION		SIGNIFICANCE (%) (6)
	μ_l (mas century ⁻¹) (2)	μ_b (mas century ⁻¹) (3)	Speed (km s ⁻¹) (4)	Axis (deg) (5)	
Piatek et al. (2002)	32 ± 13	33 ± 13	2.5 ± 0.4	112 ± 8	10
Dinescu et al. (2004)	-13 ± 16	34 ± 16	1.2 ± 0.4	116 ± 12	74
	-52	$+41$	0.2	...	100

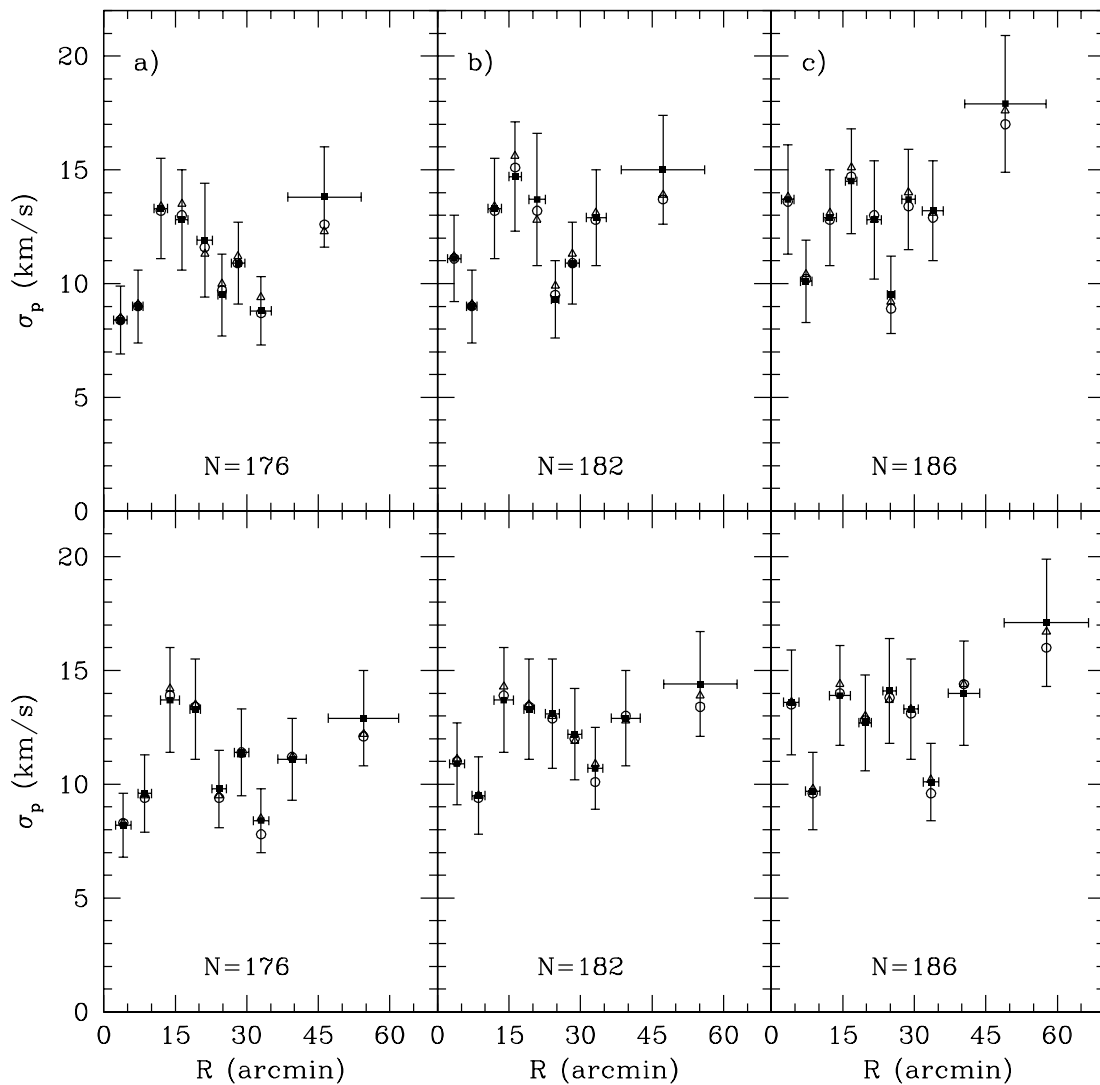


FIG. 5.—Radial velocity dispersion as a function of angular radius for three levels of Fornax membership discrimination (see § 3.2). Filled squares and error bars correspond to HRF radial velocity dispersion. Open triangles and open circles indicate the GRF radial velocity dispersion calculated using, respectively, the Piatek et al. (2002) and Dinescu et al. (2004) values for Fornax’s proper motion. The plots in the top row are constructed using circular annuli, while those in the bottom row use elliptical annuli with $\epsilon \equiv 1 - b/a = 0.3$, semimajor axis $a = R$, and P.A. = 41° . (a) Calculated using only the 176 stars with velocities surviving all four iterations of the biweight rejection algorithm. (b) Calculated using the 182 stars with velocities surviving the first two rejection iterations. (c) Calculated using the 186 stars with velocities surviving the first rejection algorithm. Bins contain approximately equal numbers of stars.

3.4.2. Velocity Dispersion Profile

To examine the velocity dispersion as a function of radius, we divide the face of Fornax into nine annuli containing approximately equal numbers (19–21 per annulus) of member stars. From the stars in each annulus, we estimate the intrinsic radial velocity dispersion using the maximum likelihood technique described above; here we modify the procedure, however, so that the estimated mean true velocity, $\langle \hat{u} \rangle$, of all bins is fixed at the value obtained from the global, unbinned sample. Since Fornax has a measured ellipticity of 0.3 ± 0.01 (IH95), we estimate the profiles using elliptical as well as circular annuli. The resulting radial velocity dispersion profile estimate, $\hat{\sigma}_p(R)$, for each of the three levels of Fornax membership rejection is shown in Figure 5. The profiles using circular annuli display more scatter than those with elliptical annuli, although in general all are consistent with a flat profile to the limit of the sampled region.

In addition to raising the overall dispersion, relaxing the membership criteria for the $N = 182$ and $N = 186$ samples empha-

sizes an upturn in the dispersion at the outermost annulus. This feature persists when varying both the shape and number of annuli and is not likely an artifact of the HRF apparent rotation signal (Fig. 4a). To demonstrate this last point, we consider the outermost circular annulus from the $N = 182$ velocity dispersion profile (Fig. 5b). This annulus contains 21 stars, spanning projected radii between $37'$ and $67'$, and has, in units of km s^{-1} , $(\langle \hat{u} \rangle, \hat{\sigma}_p) = (53.0 \pm 3.4, 15.0 \pm 2.4)$. The eight stars to the northeast of the HRF apparent rotation axis (§ 3.3) have $(\langle \hat{u} \rangle, \hat{\sigma}_p) = (55.3 \pm 5.0, 13.9 \pm 3.6)$, while the 13 stars to the southwest have $(\langle \hat{u} \rangle, \hat{\sigma}_p) = (48.1 \pm 4.1, 14.8 \pm 3.0)$. The nine stars from the latter group that are located nearest the southwest corner of Figure 2b have $(\langle \hat{u} \rangle, \hat{\sigma}_p) = (47.5 \pm 5.4, 16.1 \pm 3.9)$. In each of these subannular regions the local velocity dispersion is equal (within statistical uncertainties) to the velocity dispersion measured for the whole annulus. Thus, the adoption of a fixed mean velocity over the entire profile has not significantly inflated the calculated dispersion even where the effects of a velocity gradient would be strongest. Rather, the dispersion measured at large

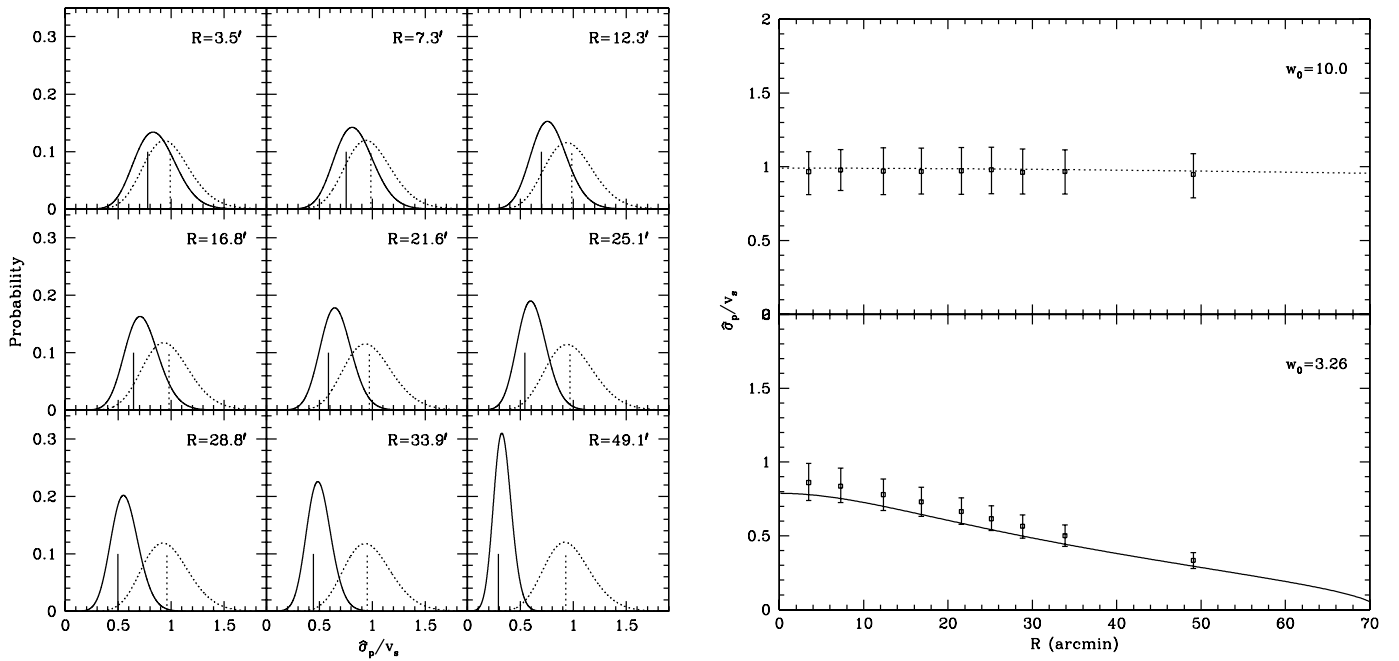


FIG. 6.—Test for bias in the velocity dispersion estimate, $\hat{\sigma}_p$, with respect to the projected velocity dispersion calculated directly from a model distribution function. *Left*: Nine panels representing the annuli (with specified angular radius) of velocity dispersion profiles calculated from simulated data. Lines indicate the probability of measuring a velocity dispersion $\hat{\sigma}_p$ in each annulus, given 1000 simulated data sets drawn from a King model with $W_0 = 3.26$ (solid line) or $W_0 = 10.0$ (dotted line). The vertical line identifies the velocity dispersion calculated directly from the corresponding model DF. *Right*: Open squares indicate the median simulated $\hat{\sigma}_p$ in each annulus. Error bars enclose the 68% of simulated $\hat{\sigma}_p$ values nearest the median. Lines represent the projected velocity dispersion calculated directly from the model DF.

radius is dominated by localized velocity scatter. The possible rise, or at the very least the lack of a falloff, in the outer dispersion may place Fornax in contrast with the Draco and Ursa Minor dSphs, for which velocity dispersion profiles have recently become available (Wilkinson et al. 2004, hereafter W04; see § 5.2).

D. N. C. Lin & S. Dong (2006, in preparation) point out that a perspective-induced HRF radial velocity gradient may produce a discrepancy between HRF and GRF radial velocity dispersion, particularly at large radii. Overplotted without error bars in Figure 5 are the GRF radial velocity dispersion profiles measured after applying equations (5) and (6) to place the individual HRF velocities in the GRF, using either of the existing Fornax proper-motion measurements. In all annuli the GRF velocity dispersion lies well within the 1σ uncertainty region of the HRF dispersion. We conclude that for the present data set, the HRF radial velocity dispersion profile is a suitable surrogate for the GRF profile.

3.4.3. Bias in the Velocity Dispersion Estimate?

By adopting equation (7) to estimate velocity dispersion, we implicitly assume that the stellar velocities everywhere follow a Gaussian distribution. This cannot strictly be correct, as tidal fields will strip high-velocity stars and internal interactions will alter the velocity distribution with time.

If the true stellar distribution function (DF) is non-Gaussian, the velocity dispersion estimate, $\hat{\sigma}_p(R)$, may deviate systematically from the true velocity dispersion profile, properly calculated as the velocity moment of the stellar DF.

To investigate the bias likely to be present in our estimate $\hat{\sigma}_p(R)$ with respect to the profile calculated from a model DF, we again perform Monte Carlo simulations. For a given model we generate 1000 artificial data sets, each comprising stellar radial velocities for 186 stars occupying the same sky positions as the stars in our observed data set. The radial velocity assigned to each star is drawn randomly from the appropriate DF, integrated at each projected radius. For individual radial velocity uncer-

tainties we adopt the same values as calculated for the observed sample in § 2.3. We bin each artificial data set, using circular annuli of the same radii and size as those in the observed $N = 186$ data set. Within each annulus, we then calculate the velocity dispersion estimate, $\hat{\sigma}_p$, and the associated confidence interval for each of the 1000 subsamples. We sum the results to obtain a function that gives the probability of measuring a given $\hat{\sigma}_p$ within that annulus, in the case that Fornax adheres to the adopted model DF. We then compare to the velocity dispersion calculated directly from the model DF.

One example of a plausible non-Gaussian DF is given by King (1962, 1966; Binney & Tremaine 1987, hereafter BT87). The King model has radius and velocity scale parameters r_s and v_s , as well as a third parameter, W_0 , that specifies the value of the central potential in units of v_s^2 . In our simulations we adopt King models with $W_0 = 3.26$ and 10.0 . These provide reasonable single-component fits to the surface brightness and flat velocity dispersion profiles, respectively. The latter model is also close to an isothermal sphere and so should have little distortion with respect to a Gaussian DF. In both cases we set $r_s = 13.7$ (IH95) and leave v_s as a free parameter.

Figure 6 shows the resulting probability functions for $\hat{\sigma}_p$ within each annulus and identifies the model projected velocity dispersion at the radius of the annulus. The projected velocity dispersion for the nearly Gaussian $W_0 = 10.0$ model lies near the center of the simulated $\hat{\sigma}_p$ distribution in each annulus. For $W_0 = 3.26$, the simulated $\hat{\sigma}_p$ values are slightly biased in favor of overestimating the model dispersion. The discrepancy between the $W_0 = 3.26$ model velocity dispersion and the median simulated $\hat{\sigma}_p$ ranges from $0.04v_s$ at the outermost annulus to $0.08v_s$ at the innermost. Since v_s roughly equals the central velocity dispersion, this discrepancy amounts to $\sim 1 \text{ km s}^{-1}$ for a dSph-like system.

We conclude that, despite the formal distinction between the estimated velocity dispersion profile, $\hat{\sigma}_p(R)$, and the projected

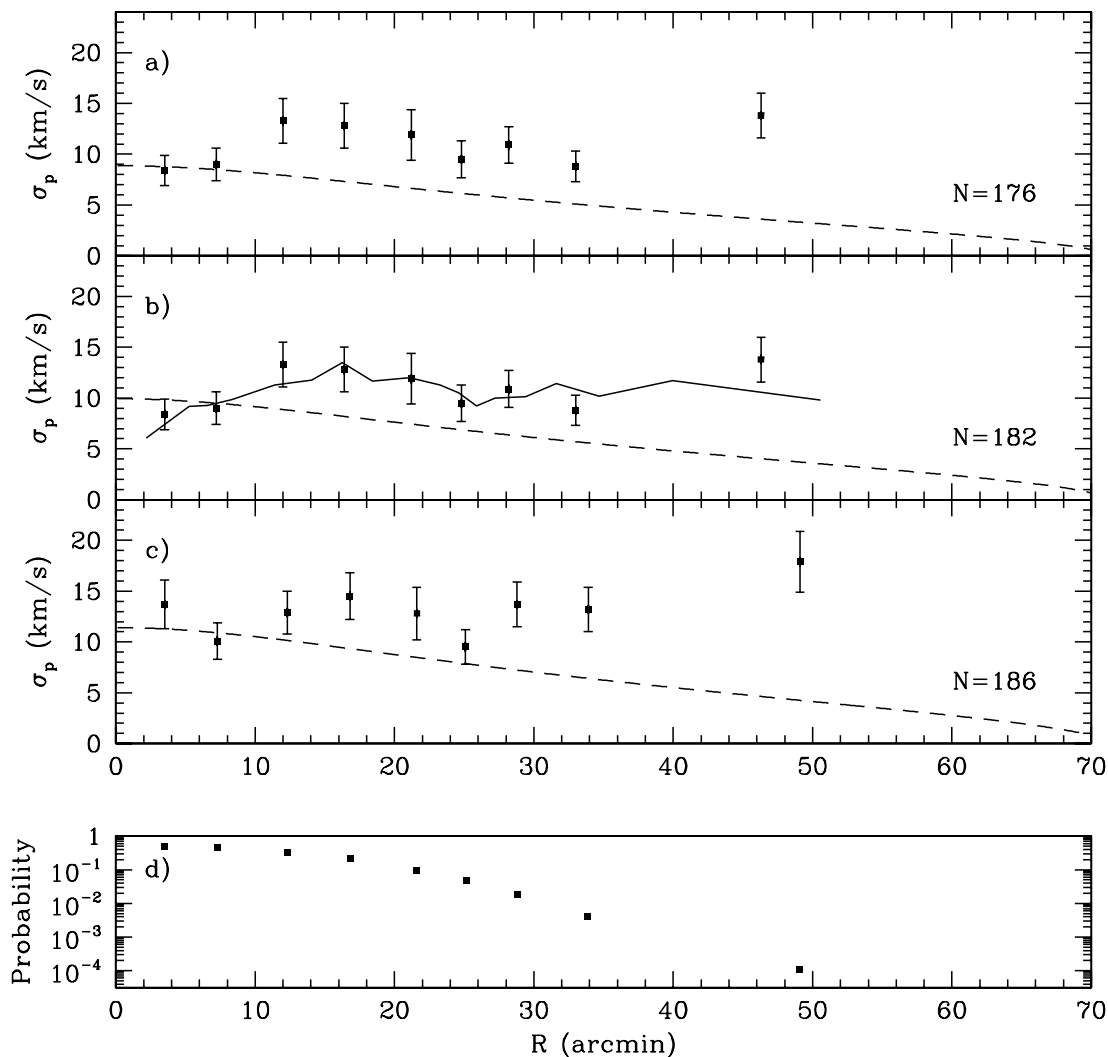


FIG. 7.—(a–c) Projected velocity dispersion from a mass-follows-light King model ($W_0 = 3.26$, $r_s = 13'.7$; IH95), drawn as a dashed line over the measured $\hat{\sigma}_p(R)$ (using circular annuli), for each of three Fornax membership samples. The solid line in (b) is the velocity dispersion estimator of Paper I (see § 4.2), which was calculated using this Fornax sample. (d) Plotted for each annulus is the probability, from simulated data drawn from the mass-follows-light King DF, of measuring a velocity dispersion at least as large as the velocity dispersion of the innermost annulus.

velocity dispersion profile calculated from a model DF, the former provides an unbiased estimate of the latter in the case of a Gaussian DF. With respect to non-Gaussian DFs, $\hat{\sigma}_p(R)$ may introduce a bias, and one should exercise caution when comparing $\hat{\sigma}_p(R)$ to such models.

4. ANALYSIS

4.1. Equilibrium Models

The classical analysis of dSph velocity data sets has relied on application of equilibrium models falling under the purview of the core-fitting technique (Richstone & Tremaine 1986). Chief among these is the single-component King model, which parameterizes the stellar DF under characteristic assumptions of dynamic equilibrium, spherical symmetry, velocity isotropy, and a mass profile that is directly proportional to the luminous profile (“mass follows light”). While they may provide a reasonable approximation of dSph cores, none of these assumptions are easily justified over the extended regions sampled by modern data sets. The Milky Way dSphs have measured ellipticities ranging from 0.13 to 0.56 (IH95). The degree to which ongoing tidal interactions with the Milky Way cause departures from

equilibrium is controversial and poorly constrained. The presence of velocity anisotropy results in a well-known degeneracy with mass. Setting aside modifications to Newtonian gravity, on no other galactic scales does mass follow light (BT87; Kormendy & Freeman 2004).

The velocity dispersion profile we measure for Fornax provides compelling evidence that the classical analysis is insufficient. A single-component King model that assumes that mass follows light has, adopting the photometrically determined Fornax structural parameters of IH95, $W_0 = 3.26$ and $r_s = 13'.7$ (Figs. 7a–7c). The artificial data sets described in § 3.4.3 indicate that, for $W_0 = 3.26$, the distribution of simulated $\hat{\sigma}_p$ values shifts to lower velocity dispersion toward larger angular radius (Fig. 6). The median simulated $\hat{\sigma}_p$ in the outermost annulus drops to one-third the median simulated $\hat{\sigma}_p$ in the innermost annulus. We do not see evidence of this behavior in the actual data, for which the measured velocity dispersion profile remains approximately flat at all radii. In none of the three Fornax membership samples is the outermost measured $\hat{\sigma}_p$ less than the innermost measured $\hat{\sigma}_p$. We use the simulated $\hat{\sigma}_p$ probability function in each annulus to calculate a negligible probability of measuring a flat velocity dispersion profile given the mass-follows-light model. Figure 7d

plots, for each annulus in the velocity dispersion profile, the probability (from the simulated $\hat{\sigma}_p$ distribution) that $\hat{\sigma}_p$ is at least as large as the median simulated $\hat{\sigma}_p$ in the innermost annulus. The probability drops from 4% for the annulus at $R = 25.1$ to 2% at $R = 28.8$, then falls by an order of magnitude at each of the two remaining annuli. We thus find a general failure of the single-component mass-follows-light King model to reproduce the flat behavior of the observed velocity dispersion profile.

It is clear that *at least* one of the classical assumptions is invalid in Fornax. Perhaps the most readily discarded is mass follows light; indeed, a flat velocity dispersion profile may arise if the stars orbit inside a dark matter halo with core radius larger than that of the visible component. We explore this scenario using two-component King models that continue to assume spherical symmetry, dynamic equilibrium, and velocity isotropy. These models contain the additional assumption of energy equipartition in the core region, which does not readily pertain to collisionless systems such as dSphs. We therefore adopt an approach similar to that of Pryor & Kormendy (1990), who used two-component King models merely as tools for exploring possible dark matter distributions in the Draco and Ursa Minor dSphs.³ If $E = -v^2/2 - \phi$ is the total energy per unit mass and ϕ is the potential per unit mass, then for the isotropic case each component i has energy distribution function (King 1966; Pryor & Kormendy 1990)

$$f_i(E) \propto e^{-\mu_i(E-v_s^2)W_0/v_s^2} - 1. \quad (11)$$

Two additional parameters join the familiar r_s , v_s , and W_0 . For luminous (subscript L) and dark (subscript D) components, ρ_{0D}/ρ_{0L} and μ_D/μ_L specify the ratios of central densities and dimensionless “masses,” respectively. The μ_i have a physical interpretation when multicomponent models are applied to stellar mass classes in globular clusters (e.g., Gunn & Griffin 1979; Da Costa & Freeman 1976). There, for mass class i , $\mu_i = m_i/\bar{m}$, where \bar{m} is the sum of $\rho_0^{-1}\rho_{0i}m_i$ over all mass classes. For our purposes, μ_D/μ_L determines the ratio of core radii, r_{cD}/r_{cL} , given energy equipartition in the core. The “core radius,” r_{ci} , is defined as the radius at which the projected density of component i falls to half its central value.

We subject each model first to constraints set by the structural parameters derived from the *single*-component King fit of IH95. We adopt $r_{cL} = 390 \pm 36$ pc (updated for a Fornax distance of 138 kpc) and $\Sigma_0 = 15.7 \pm 5.1 L_\odot \text{pc}^{-2}$ in the V band. The model surface brightness profile, $\Sigma(R)$, is scaled by the product $r_s\rho_0(M/L)_L^{-1}$, where $\rho_0 = \rho_{0D} + \rho_{0L}$ and $(M/L)_L$ is the V -band mass-to-light ratio of the luminous component, assumed to be independent of radius. For a given model, we assign the value of r_s to be that which places r_{cL} at the IH95 value. We then assign $\rho_0(M/L)_L^{-1}$ the value that recovers the IH95 value for the central surface brightness.

The models are next constrained by the available velocity dispersion and surface brightness profiles. The values of r_s and $\rho_0(M/L)_L^{-1}$ set the velocity scale according to $9v_s^2 = 4\pi Gr_s^2\rho_0$ (King 1966). For a given value of W_0 and an adopted $(M/L)_L$, we

determine the $(\rho_{0D}/\rho_{0L}, r_{cD}/r_{cL})$ pair that provides the best fit to the IH95 surface brightness profile while having a central velocity dispersion equal to the global velocity dispersion of the Fornax sample. Of these models we consider those with velocity dispersion profiles remaining flat over the sampled Fornax region to provide the best overall agreement with the data. Thus, we are approximating the observed velocity dispersion profiles of Figure 5 as perfectly flat and ignoring any bias in $\hat{\sigma}_p(R)$ with respect to the model velocity dispersion profile. We find that the favored models tend to have large W_0 values, for which such bias is expected to be minimal (§ 3.4.3).

Models representing $(M/L)_L = 1, 2, 3$ and a range of W_0 are summarized in Table 6. The first column gives the number of stars considered to be members in the velocity sample. The next six columns list the adopted $(M/L)_L$ and model parameters. The eighth column gives χ^2 per degree of freedom with respect to the velocity dispersion profile. We do not use the χ^2 test to determine a “best-fit” model, but merely to indicate the degree to which the considered models are consistent with a flat dispersion profile. The final three columns list the derived quantities of interest: the central dark matter density, total mass, and overall V -band M/L . Projected velocity dispersion and surface brightness profiles for these models are plotted in Figure 8. For simplicity we include only those models used with the $N = 182$ Fornax sample.

The available Fornax velocity data place several broad constraints on the two-component models. First, ρ_{0D} must be of order ρ_{0L} or larger in order to recover the observed central velocity dispersion. This is best illustrated by the “two”-component models with $\rho_{0D}/\rho_{0L} = 0$ (Fig. 8a). These models contain no dark matter and are therefore equivalent to the single-component, $W_0 = 3.3$ King model fit of IH95. Even if $(M/L)_L = 3$, models lacking a dark component underpredict the central velocity dispersion by a factor of 2 and fare much worse at larger radii. Thus, it is difficult to explain the velocities of even the most central stars without invoking dark matter. Recognizing that $\rho_{0L} \propto (M/L)_L$, the models able to reproduce the data have central dark matter densities between 0.04 and 0.10 $M_\odot \text{pc}^{-3}$. This is similar to the model-independent lower limit of $\rho_{0D} \geq 0.05 M_\odot \text{pc}^{-3}$, derived by Pryor & Kormendy for Draco and Ursa Minor.

Second, the models able to reproduce the data span a surprisingly narrow range in size of the dark halo, with $2 \leq r_{cD}/r_{cL} \leq 3$. The observed surface brightness profile helps set a W_0 -dependent lower limit on r_{cD}/r_{cL} . For models with $W_0 > 3.3$ (i.e., models for which the central potential is deeper than a single-component fit to the luminous material would suggest), the shape of the luminous density profile is sensitive to the dark matter potential. If r_{cD}/r_{cL} is sufficiently greater than unity, the dark matter density is constant over a few r_{cL} , and the luminous profile retains its shape even when increasing W_0 or ρ_{0D} . To demonstrate the disruptive effect of low r_{cD}/r_{cL} on the surface brightness profile, the dashed line in the bottom panel of Figure 8d is the surface brightness profile for a model with $r_{cD}/r_{cL} = 1.1$.

The apparent upper limit on r_{cD}/r_{cL} may be a consequence of the assumption that the luminous and dark components are dynamically coupled. Under equation (11), the rate at which ρ_i/ρ_0 , the density fraction of component i , decreases with radius is determined by the value of $\mu_i W_0$. The density fraction for a component with large $\mu_i W_0$ declines sharply. For large r_{cD}/r_{cL} , a model must have $\mu_L W_0$ sufficiently larger than $\mu_D W_0$. However, in the limit of small ρ_{0D}/ρ_{0L} , $\mu_L \sim 1$ as $\mu_L/\mu_D \rightarrow \infty$. Compared to the much less luminous Draco and Ursa Minor, Fornax favors models with smaller ρ_{0D}/ρ_{0L} at smaller W_0 . This tends to suppress $\mu_L W_0$, thereby preventing the luminous density profile from becoming much steeper than the dark matter profile.

³ For an approach that does not assume energy coupling between the luminous and dark matter, see Wilkinson et al. (2002), who use self-consistent stellar DFs to describe stars acting as tracers in a dark plus luminous potential. Wilkinson et al. (2002) and Pryor & Kormendy (1990) also allow for velocity anisotropy, whereas we consider only idealized, isotropic DFs. Radial velocity samples of the present size are only marginally able to address issues of anisotropy (Wilkinson et al. 2002), and we reserve a more comprehensive analysis for future work with larger data sets.

TABLE 6
PARAMETERS AND DERIVED VALUES FROM EXAMPLE TWO-COMPONENT KING MODELS

N^a	$(M/L)_L^b$ ($M_\odot L_\odot^{-1}$)	W_0	ρ_{0D}/ρ_{0L}	r_{cD}/r_{cL}	r_s (pc)	v_s (km s $^{-1}$)	χ^2/dof	ρ_{0D} ($M_\odot \text{pc}^{-3}$)	M_D^c ($10^8 M_\odot$)	M/L^d ($M_\odot L_\odot^{-1}$)	
176.....	1	3.3	0.0	...	512	5.5	19	0.0	0.00; 0.00	1; 1	
	1	3.3	3.5	1.7	772	17.5	2.2	0.067	2.3; 2.2	17; 16	
	1	5.0	3.2	2.1	775	17.0	1.6	0.061	4.4; 3.7	31; 27	
	1	7.0	3.1	2.2	732	15.8	1.5	0.059	6.5; 4.1	46; 30	
	1	9.0	3.2	2.3	722	15.7	1.6	0.060	11.0; 4.4	74; 31	
	2	3.3	0.0	...	512	7.8	13	0.31	0.00; 0.00	2; 2	
	2	3.3	1.4	1.8	729	17.1	2.5	0.053	2.0; 2.0	15; 15	
	2	5.0	1.2	2.3	717	16.1	1.7	0.046	3.8; 3.4	28; 26	
	2	7.0	1.2	2.6	683	15.3	1.6	0.046	5.8; 4.4	42; 32	
	2	9.0	1.2	2.5	639	14.4	1.5	0.046	7.4; 4.3	52; 32	
	3	3.3	0.0	...	512	9.6	10	0.47	0.00; 0.00	3; 3	
	3	3.3	0.8	1.5	632	15.8	3.4	0.046	1.2; 1.2	12; 12	
	3	5.0	0.7	2.0	610	14.8	2.0	0.040	2.4; 2.3	18; 18	
	3	7.0	0.6	2.5	589	13.9	1.7	0.035	4.1; 3.2	27; 24	
182.....	1	3.3	4.3	1.8	852	20.9	2.3	0.082	3.8; 3.6	27; 26	
	1	5.0	4.2	1.9	760	18.5	1.8	0.080	5.1; 4.2	35; 30	
	1	7.0	4.1	2.2	766	18.5	1.7	0.078	9.3; 5.6	67; 41	
	1	9.0	4.3	2.1	709	17.4	1.7	0.082	14.6; 5.9	98; 35	
	2	3.3	1.8	1.9	791	20.0	2.5	0.069	3.2; 3.1	24; 24	
	2	5.0	1.7	2.1	726	18.1	2.0	0.065	4.7; 4.2	34; 30	
	2	7.0	1.6	2.4	699	17.1	1.7	0.061	7.2; 5.2	52; 38	
	2	9.0	1.6	2.6	681	16.6	1.6	0.061	10.5; 5.8	76; 42	
	3	3.3	1.1	1.7	681	18.3	3.3	0.064	2.0; 2.0	15; 15	
	3	5.0	0.9	2.1	654	16.8	2.1	0.052	3.6; 3.3	27; 24	
	3	7.0	0.8	2.7	644	16.0	1.7	0.046	6.1; 4.8	45; 36	
	3	9.0	0.8	2.9	620	15.5	1.6	0.046	8.5; 5.4	60; 39	
	186.....	1	3.3	5.1	1.8	857	22.6	2.1	0.097	4.4; 4.2	32; 30
		1	5.0	4.9	2.0	778	20.2	1.7	0.093	6.2; 5.0	43; 36
1		7.0	4.8	2.1	750	19.3	1.5	0.092	10.0; 5.8	70; 42	
1		9.0	5.0	2.1	722	18.9	1.6	0.095	18.0; 5.9	120; 41	
2		3.3	2.1	2.0	835	22.2	2.2	0.080	4.2; 4.1	32; 30	
2		5.0	2.1	2.1	736	19.6	1.8	0.080	5.6; 4.8	40; 36	
2		7.0	2.0	2.2	694	18.2	1.6	0.076	8.0; 5.6	56; 40	
2		9.0	2.0	2.4	684	17.9	1.5	0.076	12.6; 6.2	86; 44	
3		3.3	1.3	1.8	725	20.4	2.7	0.075	2.8; 2.8	21; 21	
3		5.0	1.1	2.3	703	18.9	1.9	0.063	5.1; 4.6	36; 36	
3		7.0	1.1	2.7	687	18.4	1.7	0.063	8.5; 6.6	63; 48	
3		9.0	1.1	2.7	645	17.3	1.6	0.063	10.9; 6.6	78; 48	

^a Number of member stars in Fornax sample.

^b Adopted mass-to-light ratio of the luminous component.

^c Mass of the dark component. The first value is the total mass of the dark component; the second value is the dark mass inside $r \leq 2500$ pc.

^d V -band mass-to-light ratio in solar units. The first value is the global M/L ; the second value is M/L inside $r \leq 2500$ pc.

Finally, the flat velocity dispersion profile of Fornax favors models with large W_0 . As W_0 increases, equation (11) tends toward the distribution function of a constant velocity dispersion, isothermal sphere. The flattening of the resulting velocity dispersion profile is evident in Figure 8. Models with $W_0 \geq 7.0$ remain sufficiently flat over the observed region, for any $(M/L)_L \leq 3$, and so provide the best overall agreement with the data. Models having still larger W_0 are not ruled out by the velocity data, although they eventually require larger values of $(M/L)_L$. They also become unphysical, as $M \propto r$ for very large W_0 .

Mass and V -band M/L profiles for the most suitable $W_0 = 7.0$ and 9.0 models are shown in Figure 9. The total masses derived from these models fall in the range $(4-18) \times 10^8 M_\odot$, or $(3-7) \times 10^8 M_\odot$ if we integrate the density profile only over the observed region $r < 2$ kpc. These are 1–2 orders of magnitude larger than previous mass estimates based on only central velocity dispersion data (see M91 and references therein). This dramatic increase is a consequence of the flat velocity dispersion profile.

The two-component King models suggest that if this flatness arises from stars moving isotropically inside an extended dark halo, then Fornax is very dark even over the observed region $R \leq 1^\circ$, with M/L perhaps 10–40 times larger than that of the luminous component.

4.2. Nonparametric Mass Estimation

In Paper I we introduce a nonparametric method for estimating mass distributions from photometric and radial velocity data. We assume spherical symmetry, velocity isotropy, and dynamic equilibrium. We do not assume mass follows light, nor do we adopt a parametric form for the stellar DF. Rather, we use the IH95 star count data and each velocity data point to estimate deprojected profiles for the stellar density, $f(r)$, and squared velocity dispersion, $\mu(r)$. These relate to the underlying mass, $M(r)$, via the Jeans equations (eq. [4-55] of BT87). In addition to shedding some of the classical assumptions, this technique offers the benefit of avoiding the problems inherent to binning a radial

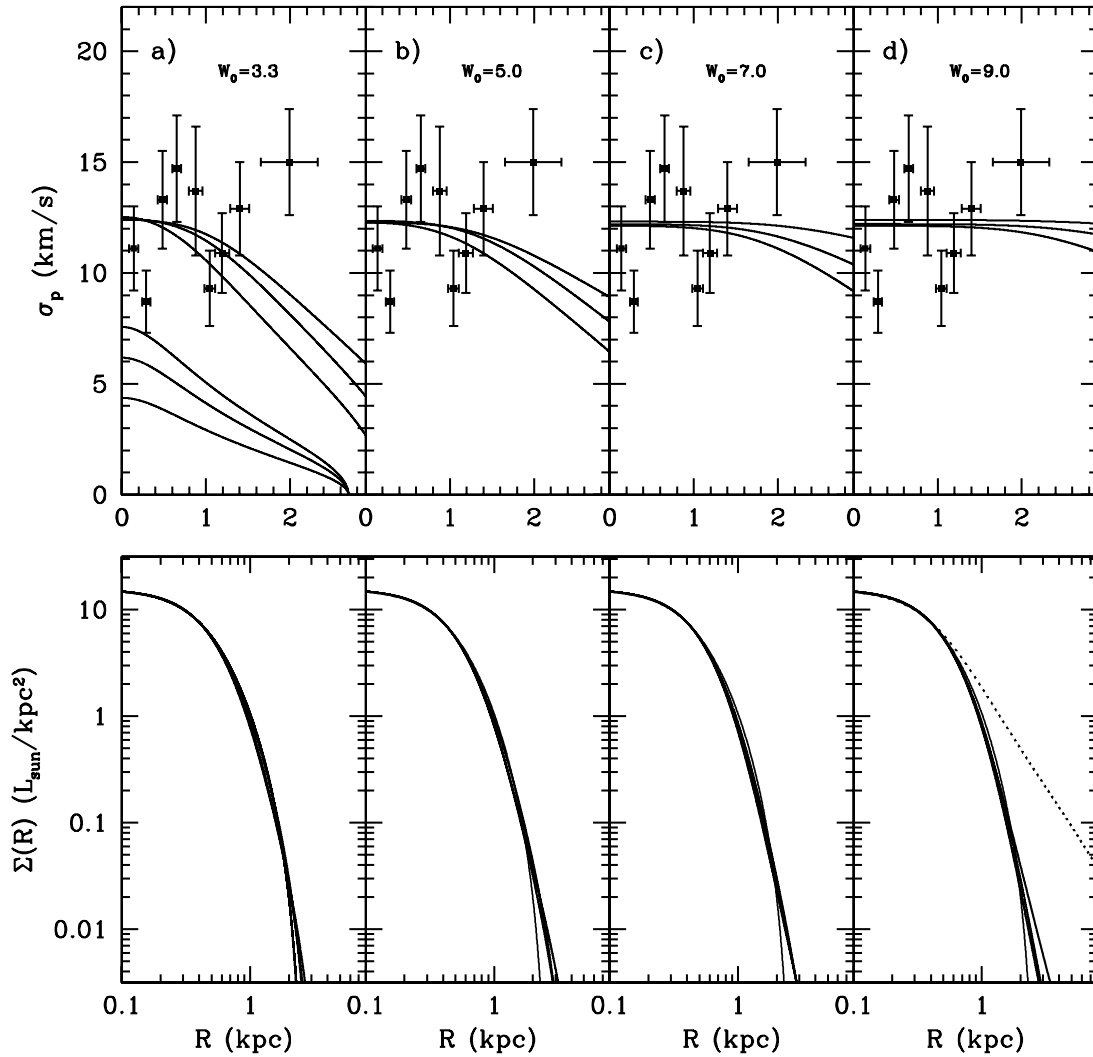


FIG. 8.—Projected velocity dispersion (*top row*) and surface brightness (*bottom row*) profiles calculated from two-component King models. From left to right, the models have increasing values for the central potential parameter, W_0 . Included in the velocity plots is the observed profile from the $N = 182$ Fornax sample. Each set of three lines corresponds to $(M/L)_L = 1, 2, 3$; $\sigma_p(R)$ falls off faster for larger $(M/L)_L$. The models at lower velocity dispersion in (*a*) have no dark matter, with $\rho_{0D}/\rho_{0L} = 0$. The thick line in the surface brightness plots is a single-component model having the IH95 structural parameters. The dotted line in the bottom panel of (*d*) represents a model with $W_0 = 9$ and $r_{cD}/r_{cL} = 1.1$ and illustrates the effect of a small core radius ratio on the surface brightness profile.

velocity data set (for a King analysis that avoids binning via maximum likelihood techniques, see Oh & Lin 1992).

Briefly, $\hat{M}(r)$ is approximated as a spline of the form

$$\hat{M}(r) = \sum_{i=1}^m \beta_i [(r - r_{i-1})_+]^p, \quad (12)$$

in which the notation $(x)_+$ indicates the greater of x or zero. The values β_1, \dots, β_m depend on $f(r)$ and $\mu(r)$ and are estimated using the available data and by imposing general shape restrictions on $\hat{M}(r)$ [e.g., $\hat{M}(r)$ is nondecreasing and $\hat{M}(r)_{r=0} = 0$]. Here we add one further shape restriction to those described in detail in Paper I. Specifically, we require the mass density to be a decreasing function of radius (see the Appendix for details). This gives a smoother $\hat{M}(r)$, eliminating the plateau features present in the original Fornax estimation (see Fig. 12 of the Appendix). Simulations indicate that a strong positive bias in the mass estimate arises beyond a radius enclosing $\sim 95\%$ of the measured stars. Inside this radius (~ 1.5 kpc for the present data set), the nonparametric technique gives $\hat{M}(r)$ accurate to within 20% when operating on data sets containing 1000 or more stellar velocities (see Fig. 7 of Paper I).

We apply the nonparametric technique to the present data set with the caveat that the uncertainty in $\hat{M}(r)$ will be at least a factor of 2. The solid line in Figure 7b is the nonparametric estimate of the velocity dispersion profile, $[\hat{\mu}(r)]^{1/2}$, obtained using the $N = 182$ Fornax sample and the star count data of IH95. The corresponding $\hat{M}(r)$ is given by the dashed line in Figure 9a. The nonparametric mass estimate has a larger central value and shallower slope than the two-component King models but displays a similar mass and behavior at radii larger than ~ 1 kpc. Figure 9b indicates that $\hat{M}(r)$ rises less steeply than the luminosity profile until approximately the Fornax core radius, where the enclosed M/L reaches a minimum value of $\sim 2 M_\odot L_\odot^{-1}$. Outside the core, dark matter dominates, reaching $M/L \sim 15 M_\odot L_\odot^{-1}$ before the estimation terminates at a radius of 1.5 kpc. Larger and more extended data sets will be of great value in taking full advantage of this technique.

4.3. External Tides

Each of the mass models, as well as the nonparametric mass estimation technique we have applied to the kinematics of Fornax, assumes that Fornax is in a state close to dynamical equilibrium.

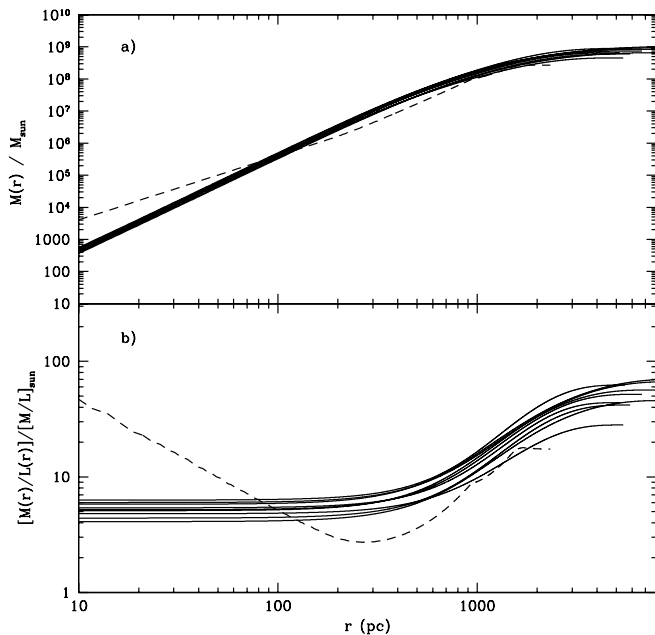


FIG. 9.—Mass and V -band M/L profiles for two-component King models from Table 6 with $W_0 \geq 7.0$. (a) Cumulative (luminous plus dark) mass profiles. (b) Cumulative mass-to-light ratio as a function of radius. The dashed lines are nonparametric estimates (§ 4.2).

This may not be valid if the dSph stellar component is tidally heated as the galaxy orbits within the Milky Way potential. Claims of member stars projected at distances well beyond the nominal tidal radius (as determined by a single-component King model fit to photometric data) of some dSphs have been cited as possible evidence for tidal influence (IH95; Martinez-Delgado et al. 2001; Palma et al. 2003; Muñoz et al. 2005). Further, the Sagittarius dSph, at a Milky Way distance of ~ 16 kpc, is clearly undergoing tidal disruption (Ibata et al. 1995, 2001; Mateo et al. 1996; Majewski et al. 2003) and so presents at least one case in which tides dominate.

Various n -body simulations have addressed the degree to which the Milky Way's tidal influence on its satellites might alter their kinematics and derived masses. Oh et al. (1995) simulate the evolution of dSphs over several perigalacticon passages and conclude that even a tidally disrupted, unbound dSph stellar population may exhibit a velocity dispersion not significantly different from its predisruption value. Piatek & Pryor (1995) simulate single perigalacticon passages and add that even when a strong tidal encounter modifies the structure and internal kinematics of a dSph, the core is least affected and the central M/L derived from the equilibrium assumption is virtually unchanged. The simulations of Klessen & Kroupa (1998) and Klessen & Zhao (2002) show that an unbound tidal remnant projected along the line of sight may display some of the kinematic and morphological features of dSphs; however, Klessen et al. (2003) later argue that the narrow horizontal branch observed in Draco rules out the ubiquity of this scenario.

The kinematic data set presented here gives an opportunity to examine certain predictions of tidal disruption models. Along a disrupting satellite's orbit, stars nearest the parent system begin to lead the satellite's center of mass as they become unbound. Since the satellite's own gravity continues to pull on these stars in the direction opposite their motion, they lose energy in the reference frame of the parent system. The opposite holds true for the satellite's stars farthest from the parent system: as they be-

come unbound, they trail the satellite's center of mass and gain energy in the parent's reference frame, since the tug from the satellite is now in the same direction as their motion. The result is elongation along the satellite's orbit and apparent rotation of the satellite about its minor axis as observed from the parent system (Piatek & Pryor 1995; Oh et al. 1995). Thus, we might expect a disrupting satellite to display two observables: a GRF rotation signal with axis of apparent rotation perpendicular to the morphological major axis, and a proper motion parallel to the morphological major axis.

For Fornax, the GRF rotation signal detected using the Piatek et al. (2002) proper motion (§ 3.3) has a rotation axis oriented nearly perpendicular to the galaxy's morphological major axis (Fig. 10). The arrows in Figure 10 show the directions and relative magnitudes of the Piatek et al. (2002) and Dinescu et al. (2004) proper-motion measurements of Fornax. The Piatek et al. (2002) proper-motion vector is clearly not aligned with the major axis, contrary to predictions from the models of tidal interaction. In contrast, the Dinescu et al. (2004) proper motion is more nearly parallel to the major axis. However, the ~ 1.2 km s $^{-1}$ GRF rotation implied by the Dinescu et al. (2004) proper motion is too slow to have statistical significance. Thus, the two observables indicative of tidal disruption are not simultaneously present in the existing kinematic data.

If we ignore the orientation of rotation and proper motion and instead simply examine the major-axis velocity trend, we find no evidence for a tidally induced velocity gradient along this axis. For a star with GRF radial velocity v , let D be the angular distance between the star and Fornax's minor axis (i.e., distance *along* the major axis), and let v_{sys} be the bulk GRF radial velocity of Fornax. We model dv/dD , the GRF radial velocity gradient along the major axis, according to $v(D) = v_{\text{sys}} + dv/dD$. This assumes that any apparent rotation resembles that of a cylindrical solid body. We then use the unbinned GRF velocity data to solve for dv/dD via linear regression. Using the Piatek et al. (2002) proper motion, we find $dv/dD \sim 0.1$ km s $^{-1}$ arcmin $^{-1}$ (3 km s $^{-1}$ kpc $^{-1}$), and the Dinescu et al. (2004) proper motion gives a shallower $dv/dD \sim 0.03$ km s $^{-1}$ arcmin $^{-1}$ (0.8 km s $^{-1}$ kpc $^{-1}$). These gradients are drawn over plots of the mean velocity along the major axis in Figure 11. The unbinned data display significant scatter about either gradient, with each fit having $\chi^2/\text{dof} \sim 30$. This contrasts with the predictions of tidal disruption models (see Fig. 7 of Piatek & Pryor 1995; Fig. 5 of Klessen & Zhao 2002), in which tides produce ordered, monotonic, and typically steeper gradients. The dispersion about either of the best-fit gradients is ~ 12 km s $^{-1}$, identical to the overall sample velocity dispersion. This indicates that the Fornax kinematics is dominated by random motions, rather than the ordered, streaming motions indicative of tidal disruption.

It should be noted that tides are not the only mechanism by which a dSph might be altered from a state of dynamic equilibrium. During a search for extratidal structure, Coleman et al. (2004, 2005) discovered two lobes along the Fornax minor axis and aligned with two shell-like features. They interpret these as signs of a recent merger event, rather than tidal tails. If a recent merger is confirmed, then there are localized regions within Fornax that have not had time to virialize, making irrelevant the concept of a virial tidal radius. To what extent such mergers may be pervasive in the dSph population remains highly uncertain, although Kleyna et al. (2003, 2004) have detected kinematically distinct substructure in Ursa Minor and Sextans. In addition, Tolstoy et al. (2004) have found evidence for two populations of ancient stars with differing metallicity *and* velocity distributions within the Sculptor dSph. It is clear that dSphs have more

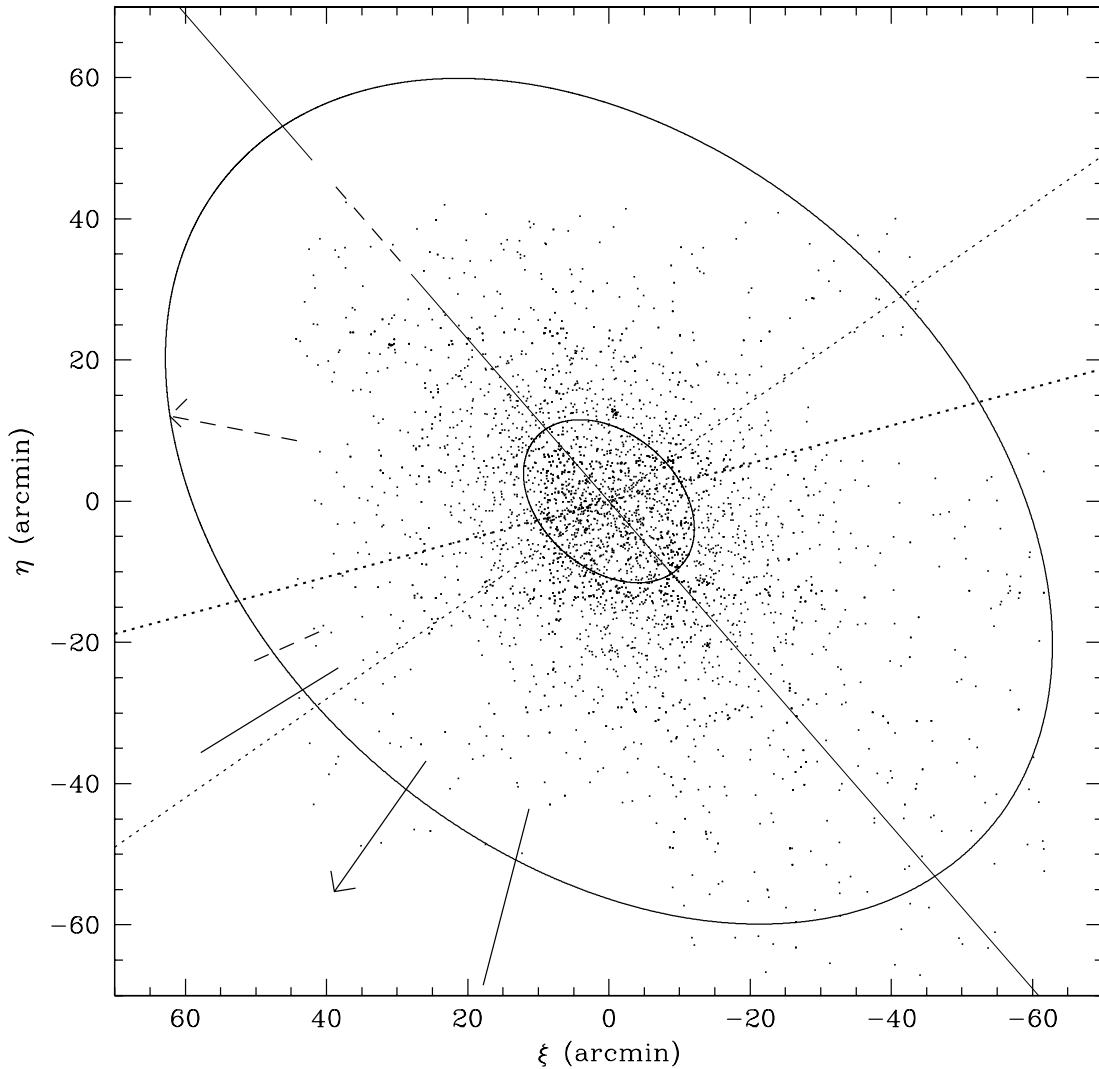


FIG. 10.—Orientation of the apparent rotation signal and published proper motion of Fornax. The solid line through (0, 0) is the Fornax morphological major axis (P.A. = $41^\circ \pm 1^\circ$; IH95), and the dotted lines through the origin enclose the probable axes of the GRF apparent rotation signal (see § 3.3). The receding hemisphere is to the northeast. Arrows indicate the direction and relative magnitude of Fornax’s proper motion in the Milky Way rest frame, as measured independently by Piatek et al. (2002; *solid arrow*) and Dinescu et al. (2004; *dashed arrow*). The associated proper-motion uncertainties are mapped conservatively, encompassing all directions allowed by the uncertainties quoted for the two components of proper motion.

complicated histories than once thought, and many more stellar spectra are required to identify distinct components.

5. DISCUSSION

5.1. Astrophysical Velocity Variability

We have assumed thus far that the measured radial velocities result exclusively from the underlying gravitational potential of Fornax. This is not necessarily true. Binary orbital motion may add a random component to any single-epoch velocity measurement, as may bulk stellar atmospheric motions.

Including the M91 data, the Fornax data set now contains multi-epoch velocity measurements for 20 stars. Having no more than five, and in most cases only two, distinct measurements for any one of these stars, we cannot deduce binary parameters. Instead we identify binary candidates as those stars exhibiting velocity variability exceeding that which we would expect from the formal measurement errors. For each multiply observed star, we calculate the χ^2_{obs} obtained from the velocity measurements and their formal errors (see Tables 3 and 4), as well as the probability, $p(\chi^2_{\text{obs}})$, that $\chi^2 \geq \chi^2_{\text{obs}}$ given Gaussian random measurement errors. These

probabilities should follow a uniform distribution between 0.0 and 1.0 if the stars are nonvariable. For our sample of 20 multiply observed stars, this would predict roughly two stars having $p(\chi^2_{\text{obs}})$ falling within each probability range 0.0–0.1, 0.1–0.2, . . . , 0.9–1.0, but only 0.02 stars having $p(\chi^2_{\text{obs}}) \leq 0.001$, which is the probability threshold suggested by Olszewski et al. (1996, hereafter OPA96) as indicative of binarity. While we do indeed find between one and three stars per each tenth in probability between 0.0 and 1.0, there are two stars (F-M20 and F2-9) for which $p(\chi^2_{\text{obs}}) \leq 0.001$. The excess over the expected number of stars at very low $p(\chi^2_{\text{obs}})$ suggests that at least these two stars are exhibiting true velocity variability and are therefore binary candidates. This implies a binary “discovery fraction” of 0.1 for the present Fornax sample.

The actual Fornax binary frequency depends not only on the fraction of observed stars we can identify as binaries, but also on the efficiency with which we can identify binaries among our subset of multiply observed stars. OPA96 perform simulations over an expanse of binary orbital parameters in order to examine the discovery efficiency for a sample of 118 stars with multiple velocity measurements in the Draco and Ursa Minor dSphs. We

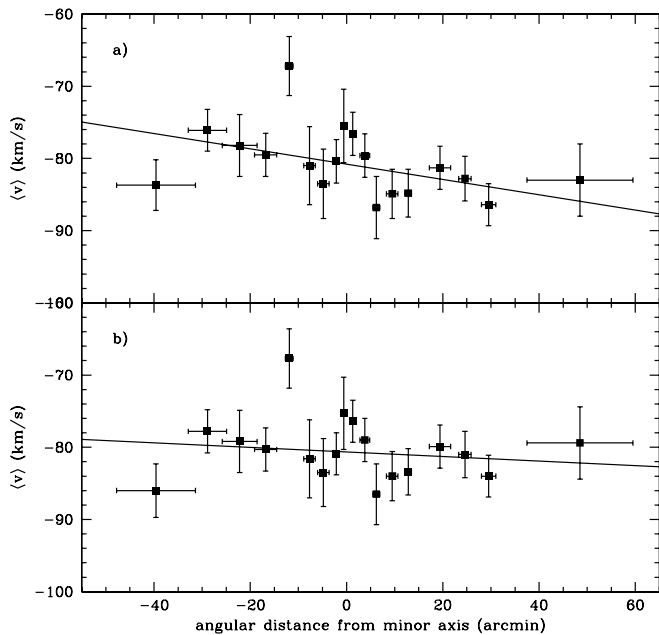


FIG. 11.—GRF mean radial velocity along Fornax’s morphological major axis. GRF velocities are calculated using Fornax proper-motion measurements by (a) Piatek et al. (2002) and (b) Dinescu et al. (2004). Solid lines represent the best-fitting radial velocity gradient, assuming cylindrical solid-body rotation.

do not attempt to replicate their procedure regarding the present Fornax sample, primarily because OPA96 have superior statistics from multiple measurements. We wish to emphasize, however, the important conclusion from OPA96 that the presence of binary stars in a dSph radial velocity sample ultimately has little effect on the derived velocity dispersion. The error in the velocity dispersion due to sampling uncertainty outweighs the error introduced by binaries. Simulations show that this result is a general feature of dSph-like velocity samples given measurement deviations similar to those in the Draco-UMi sample (Table 7 of OPA96; see also Hargreaves et al. [1996], who reach a similar conclusion from binary simulations).

A binary discovery fraction of 0.1 suggests the presence of at least 20 unidentified binaries in our Fornax velocity sample of ~ 200 stars. We make a crude attempt to examine the effect of unidentified binaries on the derived Fornax properties by observing the effects of removing the two known binaries from various subsamples of the velocity data set. First, if we calculate the velocity dispersion for the 20 stars with multiple velocity measurements, we obtain $\hat{\sigma}_{\text{multiples}} = 15.8 \pm 2.7 \text{ km s}^{-1}$. If we remove the probable binaries F-M20 and F2-9, we calculate a slightly *larger* value, $\hat{\sigma}_{\text{multiples}} = 16.4 \pm 3.0 \text{ km s}^{-1}$. Considering the velocity dispersion profile, F-M20 is in the innermost bin, and F2-9 is in the third bin. If we recalculate the velocity dispersions in these bins after the removal of the candidate binary (both bins originally contain 20 stars, so based on our binary discovery frequency, we expect at least one undetected binary to remain in each bin), we find that removal of F-M20 causes the dispersion estimate in the innermost bin to *rise* from 11.3 ± 2.0 to $11.5 \pm 2.1 \text{ km s}^{-1}$, and the removal of F2-9 causes the dispersion estimate in the third bin to rise from 13.4 ± 2.4 to $13.7 \pm 2.6 \text{ km s}^{-1}$. In both cases, inclusion of the probable binary has negligible impact on the measured velocity dispersion. We can draw no strong conclusion from these tests, as the number of detected binaries is small and the discovery efficiency is unknown. Nevertheless, we find nothing to refute the conclusion of OPA96 that binary stars negligibly inflate the measured velocity dispersion.

A second possible source of radial velocity noise may come in the form of bulk motions in the atmospheres of the observed stars (Gunn & Griffin 1979). Pryor et al. (1988) find this velocity “jitter” to be as large as $4\text{--}8 \text{ km s}^{-1}$ in globular cluster red giants, although the effect appears to fall off rapidly in stars more than 0.5 mag dimmer than the tip of the giant branch. If we define the tip of the Fornax RGB to have $I \sim 16.7$ (Fig. 1), then the region susceptible to velocity jitter includes 47 stars from the $N = 186$ Fornax sample (all but one of these stars were originally selected for spectroscopic observation prior to the observation of the photometric data set presented in § 3.1). Of these 47, 12 have repeat velocity measurements that we may examine for variability. Only one of these, F-M20, identified in the previous section as a binary candidate, has $p(\chi_{\text{obs}}^2) \leq 0.01$. While the velocity variability of the dimmer binary candidate F2-9 is unlikely to be due to atmospheric jitter, the variability of F-M20 may be due in part to atmospheric motion. The distribution of $p(\chi_{\text{obs}}^2)$ is otherwise uniform. The velocity dispersion calculated from the 47 brightest giants is $13.4 \pm 1.5 \text{ km s}^{-1}$. The velocity dispersion calculated from the remaining 139 stars from the $N = 186$ sample is $12.9 \pm 0.8 \text{ km s}^{-1}$. We conclude that atmospheric jitter does not have a significant impact on the Fornax radial velocities.

5.2. Comparison with Draco and Ursa Minor

Velocity dispersion profiles extending to the limits of the stellar distributions are now available for the dSphs Fornax, Ursa Minor, and Draco (Kleyna et al. 2002; W04; Muñoz et al. 2005). The behavior of the dispersion profiles at large radius is of great interest, capable not only of distinguishing between kinematic models but also testing assumptions on which those models are based and searching for tidal influence on the kinematics. Although the profiles are generally flat, W04 find sharp *decreases* in the velocity dispersions of both Draco and Ursa Minor at the outermost point of both profiles. The observed drops are too sudden to be explained by isotropic King or Plummer profiles. Although an abrupt change in the velocity anisotropy might explain the drop observed in Draco (see Mashchenko et al. 2005), W04 argue that anisotropy cannot by itself provide a plausible explanation for the more dramatic drop they witness in Ursa Minor. If the sharply declining dispersions in Draco and Ursa Minor are real features, they indicate an absence of tidal heating at the large radii at which they occur (Read et al. 2005). Read et al. (2005) argue that dark matter halos of up to $10^9\text{--}10^{10} M_{\odot}$ are necessary to prevent tidal heating of the stars in these dSphs. This would indicate similarity between Draco, Ursa Minor, and Fornax as described by the isotropic, two-component King models of § 4.1. It should be noted that Muñoz et al. (2005) have recently reanalyzed the data of W04 and conclude that the presence of such a drop depends largely on the binning scheme and membership criteria employed.

Regarding Fornax, we find no evidence for a decrease in the velocity dispersion at large radius for any binning scheme or reasonable membership criteria. Instead, we see some evidence for a mild increase at the outermost data point, particularly as we allow stars from the wings of the observed velocity distribution into the Fornax membership. If this rise were attributable to tidal effects, it would be puzzling that Fornax is susceptible to such external influence while Draco and Ursa Minor are not. Fornax has considerably larger luminous mass ($L_V = 1.5 \times 10^7 L_{\odot}$; Mateo 1998) and lies at a greater distance from the Milky Way (the two proper-motion studies cited in this work estimate that the current distance of $\sim 140 \text{ kpc}$ is near perigalacticon) than either Draco ($L_V = 2.6 \times 10^5 L_{\odot}$, $D = 82 \pm 6 \text{ kpc}$) or Ursa Minor

($L_V = 2.9 \times 10^5 L_\odot$, $D = 66 \pm 3$ kpc). The degree to which the Milky Way influences the kinematics of its satellites remains an open and intriguing question. The remaining Galactic dSphs, Sculptor ($L_V = 2.2 \times 10^6 L_\odot$, $D = 79 \pm 4$ kpc), Sextans ($L = 5.0 \times 10^5 L_\odot$, $D = 86 \pm 4$ kpc), Leo I ($L = 4.8 \times 10^6 L_\odot$, $D = 250 \pm 30$ kpc), Leo II ($L = 5.8 \times 10^5 L_\odot$, $D = 205 \pm 12$ kpc), Carina ($L = 4.3 \times 10^5 L_\odot$, $D = 101 \pm 5$ kpc), and the recently discovered Ursa Major dSph ($L_V \sim 4 \times 10^4 L_\odot$, $D \sim 100$ kpc; Willman et al. 2005), occupy a large region of parameter space. High-quality velocity data sets are necessary to determine any correlation between mass, orbital parameters, and the behavior of the dispersion profile at large radius.

5.3. Summary and Conclusions

We have presented new radial velocity measurements for 156 (+9 with uncertain membership status) stars belonging to the Fornax dSph. This increases the total number of Fornax stars with published velocities to 176 (+10). In order to test for rotation, we have used existing Fornax proper-motion measurements to place the heliocentric velocities in the galactic rest frame. Adoption of the Piatek et al. (2002) proper motion results in a (marginally) statistically significant GRF rotation signal of ~ 2.5 km s $^{-1}$ about an axis at $112^\circ \pm 8^\circ$, near Fornax's minor axis. Adoption of the Dinescu et al. (2004) proper motion results in no statistically significant GRF rotation signal. Despite a favorable orientation with respect to the minor axis, the rotation signal stemming from the Piatek et al. (2002) proper motion is difficult to attribute to tidal influence, as the proper-motion vector is perpendicular to Fornax's morphological major axis. Thus, the two predictions from tidal disruption models, apparent rotation about the minor axis and elongation along the satellite's orbit, are not simultaneously evident in the present data. By examining localized velocity dispersions and the velocity gradient along the major axis, we have demonstrated that the stellar kinematics of Fornax is dominated by random rather than bulk rotational or streaming tidal motions.

The Fornax radial velocity dispersion profile is generally flat. We have demonstrated the inability of single-component King models to account for the observed velocity dispersion profile. We have applied isotropic, two-component King models consistent with the observed Fornax surface brightness profile and found that models having similar central densities for dark and luminous matter are able to reproduce the flat observed velocity dispersion profile if the dark matter halo has a core of at least twice the size of the luminous material. Two-component models favored by the data have masses in the range $M \sim 10^8 - 10^9 M_\odot$. This would indicate a similarity between Fornax and the dSphs Draco and Ursa Minor, if external tides indeed do not affect the stellar kinematics in these systems. In this case, dSphs are even more massive and dark matter dominated than previously thought, which may help ameliorate the "accounting problem" faced by cold dark matter models (Klypin et al. 1999; Moore et al. 1999; Stoehr et al. 2002).

In any case, these results add to the mounting evidence that we must turn to more sophisticated analytical tools in order to explain the motions of dSph stars, particularly at large radii. We have discussed one such tool: a nonparametric statistical smoothing technique for estimating spherical masses directly from radial velocity data. An application of this method to the present Fornax sample yields a model-independent estimate of the mass profile. The result is consistent with the large Fornax masses suggested by the two-component models. This will become a powerful tool as dSph data sets continue to grow. We direct the interested reader to Paper I, in which this method is introduced in formal detail, and to the Appendix to this work.

We thank the staff at Las Campanas Observatory for support during these observing runs. We are grateful to Slawomir Piatek and Tad Pryor for valuable comments and discussion. We also thank the referee, D. N. C. Lin, for comments and criticisms that improved this work. M. M. and M. G. W. are supported in part by NSF grants AST 05-07453, AST 02-06081, and previously by NSF grant 0098661. E. O. is supported in part by NSF grants AST 00-98518, AST 02-05790, and AST 05-07453. This work also received funding from the Horace H. Rackham School of Graduate Studies at the University of Michigan, Ann Arbor (Rackham Interdisciplinary Collaboration Research Grant).

APPENDIX

Paper I modeled M by a quadratic spline,

$$\hat{M}(r) = \sum_{i=1}^m \beta_i (r - r_{i-1})_+^2, \quad (\text{A1})$$

and reduced the estimation problem to a quadratic programming problem in which a quadratic function $Q(\beta_1, \dots, \beta_m)$ is to be minimized subject to the constraints

$$\sum_{i=1}^m \beta_i = 0 = \sum_{i=1}^m \beta_i (r_m - r_{i-1}) \quad (\text{A2})$$

and

$$\sum_{i=1}^j \beta_i (r_j - r_{i-1}) \geq 0 \quad (\text{A3})$$

for $j = 1, \dots, m - 1$. These constraints are necessary for a quadratic spline to be nonnegative, nondecreasing, and bounded. Denoting the solution to the quadratic programming problem by $\hat{\beta}_1, \dots, \hat{\beta}_m$, the resulting estimator, given by equation (1),

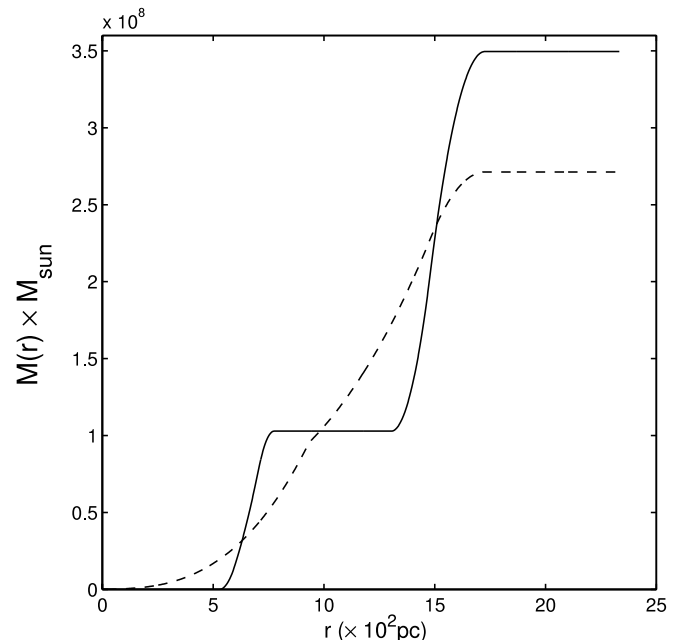


FIG. 12.—Nonparametric estimation of the Fornax mass. The solid line is the original result published in Paper I. The dashed line is the estimate produced using the same data, under the additional constraint that the mass density is a non-increasing function of radius.

tracked the gross features of (the true) M quite well in simulations, but it often has flat stretches, implying regions of no estimated mass (Fig. 12, *solid line*). The latter feature can be eliminated (as in the dashed line in Fig. 12) by supposing that the mass density $\rho(r)$ is nondecreasing in r . This assumption leads to the further constraints

$$\sum_{i=1}^j \beta_i (2r_{i-1} - r_k) \leq 0 \quad (\text{A4})$$

for $k = j - 1$ and $k = j$ for $j = 1, \dots, m$. Estimation of M with the additional assumption that ρ is nonincreasing then proceeds as in Paper I: the estimated M is given by equation (A1), where now $\hat{\beta}_1, \dots, \hat{\beta}_m$ denote the solution to the quadratic programming problem with the constraints given by equation (A4) in addition to equations (A2) and (A3).

It is also possible to estimate the density, since

$$\rho(r) = \frac{1}{4\pi r^2} M'(r),$$

where the prime denotes a derivative. For \hat{M} this becomes

$$\hat{\rho}(r) = \sum_{i=1}^m 2\hat{\beta}_i \frac{(r - r_{i-1})_+}{4\pi r^2}. \quad (\text{A5})$$

Unfortunately, equation (A5) becomes infinite as $r \rightarrow 0$, a feature that is forced by the use of quadratic splines. This is not

a fundamental problem as the total mass remains finite, nor is it unusual within the realm of widely used dynamical models [see $\rho(r)$ for the NFW model (Navarro et al. 1997), or the classical isothermal sphere].

To see how the additional constraints given by equation (A4) arise, first observe that ρ is nonincreasing if and only if

$$\frac{d}{dr} \left[\frac{1}{r^2} M(r) \right] \leq 0.$$

For M of the form given by equation (A1),

$$\frac{d}{dr} \left[\frac{1}{r^2} M(r) \right] = 2 \sum_{i=1}^j \beta_i \left(\frac{1}{r^2} - 2 \frac{r - r_{i-1}}{r^3} \right)$$

in the interval $r_{j-1} \leq r < r_j$ for $j = 1, \dots, m$. So,

$$r^3 \frac{d}{dr} \left[\frac{1}{r^2} M(r) \right] = 2 \sum_{i=1}^j \beta_i (2r_{i-1} - r)$$

in the interval $r_{j-1} \leq r < r_j$ for $j = 1, \dots, m$. Viewed as a function on the interval $[0, r_m]$, the latter is a discontinuous, piecewise linear function. So, it will be nonpositive everywhere if and only if it is nonpositive at the endpoints of each interval $r_{j-1} \leq r < r_j$.

REFERENCES

- Aaronson, M. 1983, *ApJ*, 266, L11
 Beers, T. C., Chiba, M., Yoshii, Y., Platais, I., Hanson, R. B., Fuchs, B., & Rossi, S. 2000, *AJ*, 119, 2866
 Beers, T. C., Flynn, K., & Gebhardt, K. 1990, *AJ*, 100, 32
 Bernstein, R., Shtetman, S. A., Gunnels, S. M., Mochnacki, S., & Athey, A. E. 2003, *Proc. SPIE*, 4841, 1694
 Bessell, M. S. 1976, *PASP*, 88, 557
 Binney, J., & Tremaine, S. 1987, *Galactic Dynamics* (Princeton: Princeton Univ. Press) (BT87)
 Coleman, M. G., Da Costa, G. S., Bland-Hawthorn, J., & Freeman, K. C. 2004, *AJ*, 127, 832
 ———. 2005, *AJ*, 129, 1443
 Da Costa, G. S., & Freeman, K. C. 1976, *ApJ*, 206, 128
 Dehnen, W., & Binney, J. J. 1998, *MNRAS*, 298, 387
 Dinescu, D. I., Keeney, B. A., Majewski, S. R., & Girard, T. M. 2004, *AJ*, 128, 687
 Evans, D. S. 1967, in *IAU Symp. 30, The Revision of the General Catalogue of Radial Velocities*, ed. A. H. Batten & J. F. Heard (London: Academic), 57
 Fleck, J. J., & Kuhn, J. R. 2003, *ApJ*, 592, 147
 Gunn, J. E., & Griffin, R. F. 1979, *AJ*, 84, 752
 Hargreaves, J. C., Gilmore, G., & Annan, J. D. 1996, *MNRAS*, 279, 108
 Ibata, R. A., Gilmore, G., & Irwin, M. J. 1995, *MNRAS*, 277, 781
 Ibata, R., Irwin, M., Lewis, G. F., & Stolte, A. 2001, *ApJ*, 547, L133
 Irwin, M., & Hatzidimitriou, D. 1995, *MNRAS*, 277, 1354 (IH95)
 King, I. R. 1962, *AJ*, 67, 471
 ———. 1966, *AJ*, 71, 64
 Klessen, R. S., Grebel, E. K., & Harbeck, D. 2003, *ApJ*, 589, 798
 Klessen, R. S., & Kroupa, P. 1998, *ApJ*, 498, 143
 Klessen, R. S., & Zhao, H. 2002, *ApJ*, 566, 838
 Kleyna, J. T., Wilkinson, M. I., Evans, N. W., & Gilmore, G. 2001, *ApJ*, 563, L115
 ———. 2004, *MNRAS*, 354, L66
 ———. 2005, *ApJ*, 630, L141
 Kleyna, J. T., Wilkinson, M. I., Evans, N. W., Gilmore, G., & Frayn, C. 2002, *MNRAS*, 330, 792
 Kleyna, J. T., Wilkinson, M. I., Gilmore, G., & Evans, N. W. 2003, *ApJ*, 588, L21
 Klypin, A., Kravtsov, A. V., Valenzuela, O., & Prada, F. 1999, *ApJ*, 522, 82
 Kormendy, J., & Freeman, K. C. 2004, in *IAU Symp. 220, Dark Matter in Galaxies*, ed. S. D. Ryder, D. J. Pisano, & K. C. Freeman (San Francisco: ASP), 377
 Kroupa, P. 1997, *NewA*, 2, 139
 Kuhn, J. R. 1993, *ApJ*, 409, L13
 Majewski, S. R., Skrutskie, M. F., Weinberg, M. D., & Ostheimer, J. C. 2003, *ApJ*, 599, 1082
 Martinez-Delgado, D., Alonso-Garcia, J., & Aparicio, A. 2001, *ApJ*, 549, L63
 Mashchenko, S., Couchman, H. M. P., & Sills, A. 2005, *ApJ*, 624, 726
 Mateo, M. L. 1998, *ARA&A*, 36, 435
 Mateo, M., Mirabel, N., Udalski, A., Szymanski, M., Kaluzny, J., Kubiak, M., Krzeminski, W., & Stanek, K. 1996, *ApJ*, 458, L13
 Mateo, M., Olszewski, E., Welch, D. L., Fischer, P., & Kunkel, W. 1991, *AJ*, 102, 914 (M91)
 Moore, B., Ghigna, S., Governato, F., Lake, G., Quinn, T., Stadel, J., & Tozzi, P. 1999, *ApJ*, 524, L19
 Muñoz, R. R., et al. 2005, *ApJ*, 631, L137
 Navarro, J. F., Frenk, C. S., & White, S. D. M. 1997, *ApJ*, 490, 493
 Odenkirchen, M., et al. 2001, *AJ*, 122, 2538
 Oh, K. S., & Lin, D. N. C. 1992, *J. Korean Astron. Soc.*, 25, 1
 Oh, K. S., Lin, D. N. C., & Aarseth, S. J. 1995, *ApJ*, 442, 142
 Olszewski, E. W., Pryor, C., & Armandroff, T. E. 1996, *AJ*, 111, 750 (OPA96)
 Olszewski, E. W., Schommer, R. A., Suntzeff, N. B., & Harris, H. C. 1991, *AJ*, 101, 515
 Palma, C., Majewski, S. R., Siegel, M. H., Patterson, R. J., Ostheimer, J. C., & Link, R. 2003, *AJ*, 125, 1352
 Piatek, S., & Pryor, C. 1995, *AJ*, 109, 1071
 Piatek, S., et al. 2002, *AJ*, 124, 3198
 Pryor, C., & Kormendy, J. 1990, *AJ*, 100, 127
 Pryor, C. P., Latham, D. W., & Hazen, M. L. 1988, *AJ*, 96, 123
 Read, J. I., Wilkinson, M. I., Evans, N. W., Gilmore, G., & Kleyna, J. T. 2005, in *IAU Colloq. 198, Near-Fields Cosmology with Dwarf Elliptical Galaxies*, ed. H. Jerjen & B. Binggeli (Cambridge: Cambridge Univ. Press), 235
 Rice, J. A. 1995, *Mathematical Statistics and Data Analysis* (Belmont: Duxbury)
 Richstone, D. O., & Tremaine, S. 1986, *AJ*, 92, 72
 Schechter, P. L., Mateo, M., & Saha, A. 1993, *PASP*, 105, 1342
 Shtetman, S. A. 1984, *Proc. SPIE*, 445, 128
 Stoehr, F., White, S. D. M., Tormen, G., & Springel, V. 2002, *MNRAS*, 335, L84

- Tolstoy, H., et al. 2004, ApJ, 617, L119
- Tonry, J., & Davis, M. 1979, AJ, 84, 1511
- Udry, S., et al. 1999, in IAU Colloq. 170, Precise Stellar Radial Velocities, ed. J. B. Hearnshaw & C. D. Scarfe (ASP Conf. Ser. 185; San Francisco: ASP), 383
- Wang, X., Woodroffe, M., Walker, M. G., Mateo, M., & Olszewski, E. W. 2005, ApJ, 626, 145 (Paper I)
- Wilkinson, M. I., Kleyna, J., Evans, N. W., & Gilmore, G. 2002, MNRAS, 330, 778
- Wilkinson, M. I., Kleyna, J. T., Evans, N. W., Gilmore, G. F., Irwin, M. J., & Grebel, E. K. 2004, ApJ, 611, L21 (W04)
- Willman, B., et al. 2005, ApJ, 626, L85